

Branch-specific dendritic Ca^{2+} spikes cause persistent synaptic plasticity

Joseph Cichon¹ & Wen-Biao Gan¹

The brain has an extraordinary capacity for memory storage, but how it stores new information without disrupting previously acquired memories remains unknown. Here we show that different motor learning tasks induce dendritic Ca^{2+} spikes on different apical tuft branches of individual layer V pyramidal neurons in the mouse motor cortex. These task-related, branch-specific Ca^{2+} spikes cause long-lasting potentiation of postsynaptic dendritic spines active at the time of spike generation. When somatostatin-expressing interneurons are inactivated, different motor tasks frequently induce Ca^{2+} spikes on the same branches. On those branches, spines potentiated during one task are depotentiated when they are active seconds before Ca^{2+} spikes induced by another task. Concomitantly, increased neuronal activity and performance improvement after learning one task are disrupted when another task is learned. These findings indicate that dendritic-branch-specific generation of Ca^{2+} spikes is crucial for establishing long-lasting synaptic plasticity, thereby facilitating information storage associated with different learning experiences.

One remarkable feature of the brain is to encode and store new information continuously without disrupting previously acquired memories. It is believed that experience-dependent changes in synaptic strength are crucial for information storage in the brain^{1,2}. However, it remains unclear whether and how synaptic plasticity induced by past experiences are maintained in the face of new experiences^{1–3}. To address this question, we examined the generation of dendritic Ca^{2+} spikes and their effect on synaptic plasticity in the primary motor cortex of mice performing different motor learning tasks.

Dendritic Ca^{2+} spikes trigger large Ca^{2+} influx into dendrites^{4–8}, and have been linked to activity-dependent increases or decreases of synaptic strength in brain slices^{9–14}. Recent studies have shown that NMDA (*N*-methyl-D-aspartate)-receptor-dependent dendritic Ca^{2+} spikes are generated in several brain regions and are involved in the integration and amplification of synaptic inputs^{15–19}. The function of Ca^{2+} spikes in regulating experience-dependent synaptic plasticity in the living brain remains undetermined. Here we show that different motor tasks induce dendritic Ca^{2+} spikes on different apical tuft branches of individual layer V (L5) pyramidal neurons in the mouse motor cortex. This spatial segregation of Ca^{2+} spikes is crucial for the induction and maintenance of synaptic potentiation related to different learning tasks. These findings underscore the important role of branch-specific dendritic Ca^{2+} spikes (BSDCS) in storing new information without disrupting existing memories in the brain.

Motor learning induces BSDCS

To investigate the potential role of dendritic Ca^{2+} spikes in learning-dependent synaptic plasticity, we first examined Ca^{2+} spike generation in the motor cortex of mice using a treadmill training paradigm²⁰. In this model, head-restrained mice ran on a treadmill under a two-photon microscope and learned to change their gait patterns within 1 hour^{20,21} (Fig. 1a–c and Extended Data Fig. 1). To detect Ca^{2+} spikes, we performed two-photon Ca^{2+} imaging of apical tuft dendrites of L5 pyramidal neurons expressing genetically encoded Ca^{2+} indicators (GCaMPs) (Fig. 1d and Extended Data Fig. 2a–c). We observed a significant increase ($>700\%$) in the number of Ca^{2+} transients occurring across long stretches of dendrites in mice running on the treadmill

than in quiet awake state (Fig. 1d–f and Extended Data Fig. 2c–h). As expected²², dendritic Ca^{2+} transients detected with GCaMP6s exhibited a significantly larger $\Delta F/F_0$ but slower kinetics than with other GCaMPs (Fig. 1e and Extended Data Fig. 2d–f). The observed dendritic Ca^{2+} transients are reminiscent of NMDA-receptor-dependent Ca^{2+} spikes reported in other brain regions^{15–19} in that they typically lasted hundreds of milliseconds with comparable $\Delta F/F_0$ across long dendritic segments ($>30\ \mu\text{m}$) (Fig. 1d, e and Extended Data Fig. 2c–g). Moreover, the frequency and peak amplitude of these dendritic Ca^{2+} transients were significantly reduced in the presence of the NMDA receptor antagonist MK801 (Fig. 1g, h and Extended Data Fig. 2h, i). Together, these observations suggest that treadmill motor learning induces NMDA-receptor-dependent Ca^{2+} spikes on apical tuft branches of L5 pyramidal neurons in the motor cortex.

When mice underwent forward running (FWR) and then backward running (BWR) (five 30-s trials for each direction), of the tuft branches that spiked and were located within $100\ \mu\text{m}$ below the pial surface, $\sim 95\%$ exhibited Ca^{2+} spikes during either FWR or BWR, while only $\sim 5\%$ showed Ca^{2+} spikes during both running tasks (Fig. 1i). Furthermore, in mice trained to run in four directions, only $\sim 10\%$ of those tuft branches exhibited Ca^{2+} spikes in response to two or more tasks (Fig. 1i). Thus, different running tasks induce Ca^{2+} spikes on different tuft branches with little overlap.

In contrast to non-overlapping Ca^{2+} spikes on distal tuft branches, we observed substantial overlap of Ca^{2+} activities in apical dendritic trunks (nexus, near the base of tuft branches) and L5 somata when mice were subjected to two or four direction running (Fig. 1a, j, l and Extended Data Fig. 3a–e). This observation suggests that different motor tasks induce Ca^{2+} spikes on separate tuft branches of the same L5 pyramidal neurons. Indeed, out of 33 pairs of sibling branches located within $100\ \mu\text{m}$ below the pial surface, only 2 pairs showed FWR- and BWR-induced Ca^{2+} spikes on the same branches, whereas the remaining 31 pairs exhibited no such overlap (Fig. 1k, m and Extended Data Fig. 3h). As these higher-order tuft branches converge towards the nexus, a larger overlap of FWR- and BWR-induced Ca^{2+} spikes was observed on sibling branches located 100 – $200\ \mu\text{m}$ from the pial surface (Fig. 1l, m and Extended Data Fig. 3f, g, i, j). At this cortical depth, $\sim 16\%$ of Ca^{2+}

¹Skirball Institute, Department of Neuroscience and Physiology, New York University School of Medicine, New York, New York 10016, USA.

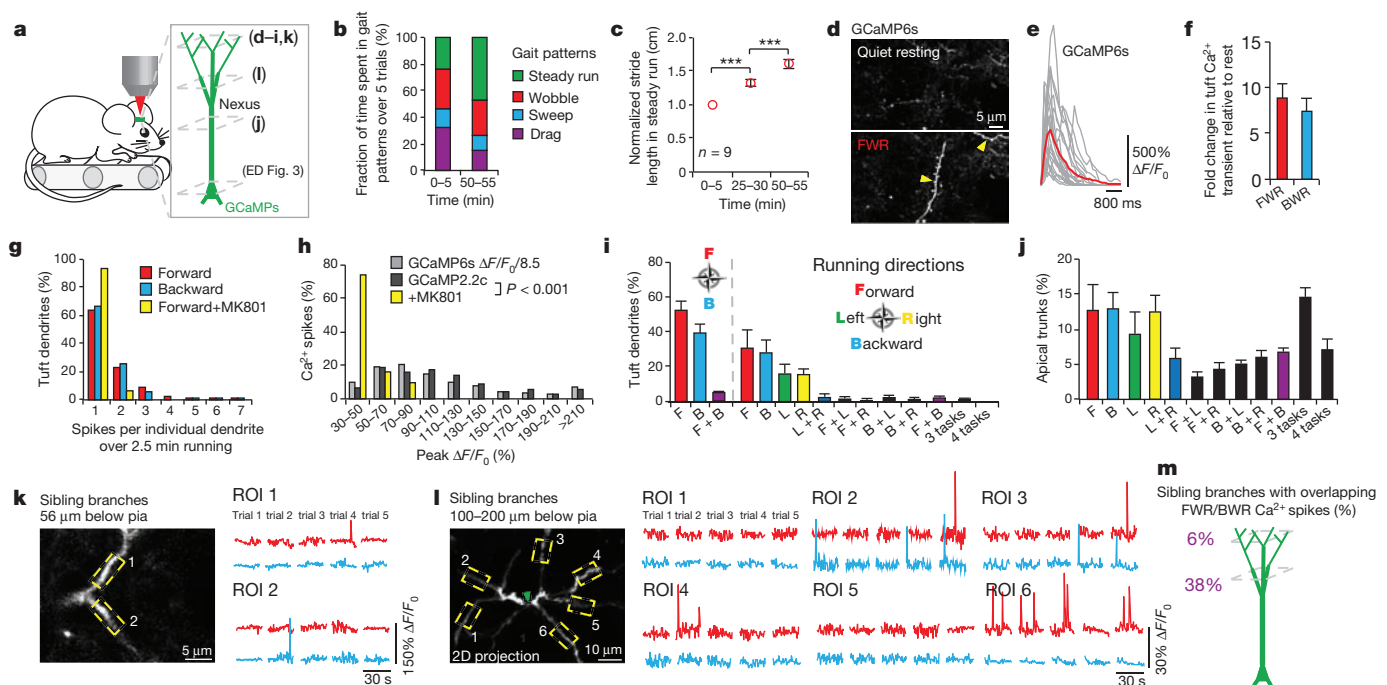


Figure 1 | Motor learning induces branch-specific Ca^{2+} spikes in apical tuft dendrites of L5 pyramidal neurons in motor cortex. **a**, Schematic of two-photon Ca^{2+} imaging at different cortical depths during treadmill training. **b**, Changes of forelimb gait patterns between early and late trials. **c**, Average stride length in steady run increased after training ($n = 9$ mice, paired t -test). **d**, Images of tuft dendrites expressing GCaMP6s during resting and FWR. Running-induced Ca^{2+} transients were visible over long dendritic segments (yellow arrowheads). **e**, Fast-scanning of individual Ca^{2+} transients (grey traces, $n = 24$) during FWR. Red trace represents the average. **f**, The number of Ca^{2+} transients increased >7 -fold during FWR or BWR relative to resting ($P = 2.6 \times 10^{-7}$, paired t -test). **g**, Distribution of Ca^{2+} spike frequency on individual branches during FWR ($n = 321$), BWR ($n = 261$) and FWR with local MK801 ($n = 34$) over 2.5 min. **h**, Distribution of peak Ca^{2+} spike

amplitudes detected with GCaMP6s and GCaMP2.2c during FWR with or without MK801 ($n = 141$, 213 and 31, respectively; $P < 0.0001$, Mann–Whitney test). $\Delta F/F_0$ values of Ca^{2+} spikes detected with GCaMP6s were ~ 8.5 times larger than with GCaMP2.2c. **i**, 95% of tuft branches that spiked were activated by only one task ($n = 616$ for two tasks; $n = 450$ for four tasks). **j**, 53% of apical trunks exhibited Ca^{2+} transients in response to several tasks ($n = 257$). **k**, Sibling branches exhibited non-overlapping FWR- and BWR-induced Ca^{2+} spikes. **l**, Two-dimensional projection of multiple sibling branches. Green arrowhead marks the trunk. Six regions of interests (ROIs) corresponding to different branches were analysed over five trials of FWR and BWR. **m**, The percentage of sibling branches with overlapping FWR/BWR-induced Ca^{2+} spikes at two cortical depths below the pia. Data are mean \pm s.e.m. *** $P < 0.001$. See Methods for statistical details.

spikes (48 out of 294 spikes) occurred simultaneously in all branches (global) of the same neuron in response to FWR or BWR (Extended Data Fig. 3k). Notably, when tuft branches from an individual neuron were cut with a two-photon laser, running-induced Ca^{2+} activity in the trunk was significantly reduced (Extended Data Fig. 4). Together, these findings indicate that different motor tasks trigger Ca^{2+} spikes in largely non-overlapping distal apical tuft branches of the same L5 pyramidal neurons (Fig. 1m, Extended Data Fig. 3j and Supplementary Information). They also suggest that Ca^{2+} spikes generated in individual tuft branches propagate along dendrites and contribute to the activity in apical trunks and somata.

Spines active during BSDCS are potentiated

Dendritic Ca^{2+} spikes have been shown to trigger long-term synaptic potentiation or depression in brain slices^{9–14}. To investigate the effect of Ca^{2+} spikes on synaptic plasticity *in vivo*, we examined Ca^{2+} activities of dendritic spines before and after Ca^{2+} spike generation. In mice subjected to FWR or BWR, Ca^{2+} transients in dendritic spines were readily detected with different GCaMP variants (Fig. 2a and Extended Data Fig. 5a–g). These running-induced spine Ca^{2+} transients sometimes coincided with the generation of Ca^{2+} spikes (Fig. 2a, b and Extended Data Fig. 5h–l). For spines active at the time of spike generation, the average ratio of GCaMP6s fluorescence intensity between spine heads and neighbouring shafts was 1.56 ± 0.13 (mean \pm s.e.m.), significantly higher than that for neighbouring inactive spines (0.46 ± 0.02) (Extended Data Fig. 5k, l; $P < 0.001$). Notably, after Ca^{2+} spikes, these active spines exhibited a significant increase in the peak amplitude of Ca^{2+} transients (Fig. 2a–c and Extended Data Fig. 5h–j, m–o; $74.7 \pm 7.3\%$ for FWR

($n = 80$) and $52.7 \pm 10.9\%$ for BWR ($n = 18$); $P < 0.001$). By contrast, no significant potentiation of Ca^{2+} transients was observed in spines that were inactive at the time of spike generation or did not experience a Ca^{2+} spike (inactive spines: $1.8 \pm 5.8\%$, $P = 0.76$, $n = 22$; no Ca^{2+} spike: $4.2 \pm 2.9\%$, $P = 0.15$, $n = 35$). We also found that the increase in the peak amplitude of spine Ca^{2+} transients was significantly correlated with the peak amplitude of Ca^{2+} spikes and the ratio of fluorescence intensity between spine heads and neighbouring shafts at the time of spike generation (Fig. 2d, e and Supplementary Information). Moreover, local infusion of MK801 or calcium/calmodulin-dependent protein kinase II (CaMKII) inhibitors into the motor cortex abolished the potentiation of Ca^{2+} transients in spines active during FWR (Fig. 2c and Extended Data Fig. 6a). Unlike MK801, CaMKII inhibition did not significantly alter Ca^{2+} spike frequency or peak amplitude (Extended Data Fig. 6b–d). Together, these results show that Ca^{2+} spikes cause the potentiation of Ca^{2+} transients in synchronously active spines via a process requiring NMDA receptor activation and CaMKII signalling.

The potentiation of Ca^{2+} transients could be observed within 6.2 ± 0.7 s after a single Ca^{2+} spike induced by FWR ($n = 60$, Extended Data Fig. 5n). When spines were examined 20–40 min after Ca^{2+} spike-induced Ca^{2+} potentiation, most spines continued to exhibit Ca^{2+} potentiation (Fig. 2f; $P < 0.001$). We further examined dendritic spine size change over time in L5 pyramidal neurons expressing both GCaMP6s and a structural marker, tdTomato (Fig. 2g, h). Most spines that exhibited Ca^{2+} potentiation immediately after Ca^{2+} spikes also showed an increase in spine size within 40 min (Extended Data Fig. 5o). The average size of spines active during Ca^{2+} spikes increased over 40 min, but not over 2 min (Fig. 2g, h; 2 min: $2.1 \pm 7.1\%$, $P = 0.77$, $n = 11$; 40 min: $32.3 \pm 11.1\%$,

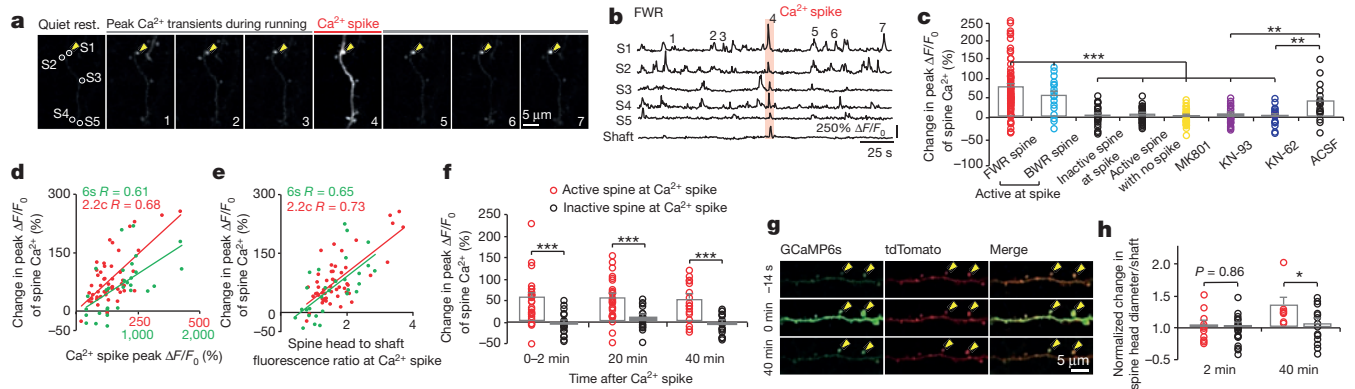


Figure 2 | Ca^{2+} spikes cause persistent potentiation of task-related dendritic spines. **a, b,** Time-lapse images and fluorescent traces of a representative apical tuft branch and spines expressing GCaMP6s. Running-induced Ca^{2+} transients in spines (arrowheads point to peak Ca^{2+} signals for spine 1) and a Ca^{2+} spike (marked by red bar). **c,** Spines active during spikes showed a significant increase in the peak amplitude of Ca^{2+} transients after Ca^{2+} spikes during FWR ($n = 80$) and BWR ($n = 18$), whereas spines not active during spikes ($P = 0.76$; $n = 22$ spines), or active spines with no encounter of spikes ($P = 0.15$; $n = 35$), showed no increase. Local application of MK801 ($n = 31$), KN-93 ($n = 20$) and KN-62 ($n = 18$), but not artificial cerebrospinal fluid (ACSF), blocked potentiation of spine Ca^{2+} transients

$P < 0.05$; $n = 8$). There was no significant increase in the size of inactive spines over 2 or 40 min (2 min: $0.6 \pm 4.5\%$, $P = 0.89$, $n = 23$; 40 min: $4.0 \pm 7.6\%$, $P = 0.61$, $n = 14$). Because spine size strongly correlates with synaptic strength^{23,24}, these findings suggest that branch-specific Ca^{2+} spikes induced by motor running tasks cause long-lasting increase in the strength of synapses that are active at the time of spike generation.

Spines active before BSDCS are depotentiated

Previous *in vitro* studies have shown that Ca^{2+} spikes can cause either synaptic potentiation or depotentiation, depending on the time interval (typically less than 1 s) between synaptic activity and Ca^{2+} spike generation^{25,26}. We therefore examined Ca^{2+} transients in spines that were active at different time intervals relative to Ca^{2+} spikes. In mice subjected to FWR, most spines (54%) exhibited activities coinciding with spike generation. In spines active asynchronously relative to Ca^{2+} spikes, the average time interval between the two events was 12.2 ± 1.6 s (Extended Data Fig. 7a, b). On the other hand, when animals were switched from FWR to BWR, many spine transients induced by FWR occurred seconds before the generation of Ca^{2+} spikes induced by BWR (Fig. 3a, b). Notably, FWR spines active within 5 s before Ca^{2+} spikes induced by BWR showed a significant reduction in the peak amplitude of Ca^{2+} transients when measured again in response to FWR (Fig. 3a–c; $-38.6 \pm 4.1\%$, $P < 0.001$; ratio of fluorescence intensity between spine heads and neighbouring shafts was 0.53 ± 0.03 during BWR-induced Ca^{2+} spikes; $n = 18$). There was no significant correlation between the degree of spine Ca^{2+} depotentiation and the peak amplitude of Ca^{2+} spikes (Fig. 3d; $R = -0.17$, $P = 0.35$). By contrast, FWR-activated spines did not show Ca^{2+} depotentiation if they were active > 5 s before spike generation or did not encounter spikes (Fig. 3c; > 5 s: $-4.9 \pm 3.4\%$, $P = 0.16$, $n = 31$; no spikes: $1.8 \pm 5.0\%$, $P = 0.66$, $n = 31$; Extended Data Fig. 7c–f). Furthermore, local application of MK801 prevented Ca^{2+} spike-induced Ca^{2+} depotentiation in FWR-activated spines (Fig. 3c; $-3.7 \pm 3.2\%$, $P = 0.26$, $n = 34$). Together, these results indicate that Ca^{2+} spikes cause spine depotentiation if spines are active within 5 s before spike generation (Supplementary Information).

It is important to note that the percentage of spines active seconds before spike generation during FWR was much smaller than that of spines active at the time of spike generation (Extended Data Fig. 7a, b). As a result, Ca^{2+} spikes cause a net potentiation rather than depotentiation in spine Ca^{2+} transients during FWR. Moreover, because FWR

($P > 0.05$). **d, e,** Change in the peak amplitude of spine Ca^{2+} transients correlates with the peak amplitude of Ca^{2+} spike (d) and the fluorescence ratio between spine head and dendritic shaft (e) for spines active at the time of spike generation during FWR ($P < 0.001$ for GCaMP6s and GCaMP2.2c, Pearson correlation). **f,** Ca^{2+} spikes induced persistent potentiation of spine Ca^{2+} transients over 40 min ($n = 28$). **g, h,** Spines undergoing Ca^{2+} spikes-induced Ca^{2+} potentiation, not neighbouring inactive spines, also showed an increase in spine head size over 40 min ($n = 8$) but not over 2 min ($n = 11$). Data are mean \pm s.e.m. * $P < 0.05$, ** $P < 0.01$, *** $P < 0.001$, paired *t*-test. See Methods for statistical details.

and BWR induce Ca^{2+} spikes on different apical tuft branches, spines potentiated during FWR rarely encountered BWR-induced Ca^{2+} spikes to get depotentiated. Thus, the generation of Ca^{2+} spikes on different branches reduces the chance that synaptic changes induced by past experiences are disrupted by new experiences.

Persistent spine potentiation relies on BSDCS

The above findings suggest that the spatial segregation of dendritic Ca^{2+} spikes could be important for maintaining experience-dependent

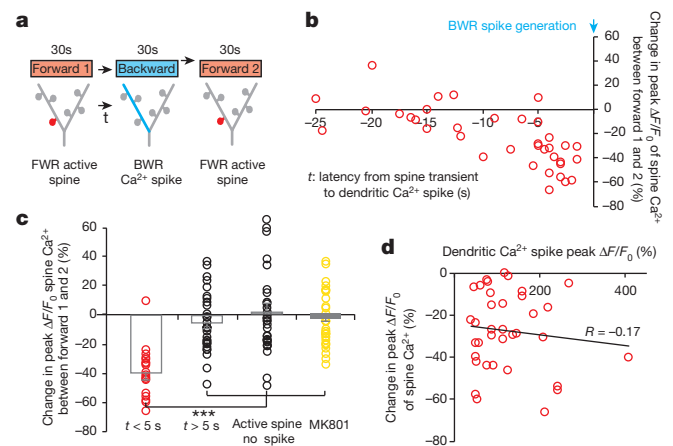


Figure 3 | Ca^{2+} spikes depotentiate spines active seconds before spike generation. **a,** A task-switching protocol for inducing spine activity and Ca^{2+} spike asynchronously. **b,** Changes in the peak amplitude of Ca^{2+} transients in FWR-activated spines versus the time interval between spine activity and a BWR-induced Ca^{2+} spike. **c,** Changes in the peak amplitude of spine Ca^{2+} transients under various conditions. Spines active within 5 s before the spike generation show a significant reduction in the peak amplitude of Ca^{2+} transients when measured again during FWR training ($n = 18$ spines), whereas spines active > 5 s before the spike ($n = 31$ spines) or active spines without encountering spikes ($n = 31$ spines) showed no reduction. Local application of MK801 blocked the reduction. **d,** No correlation between the percentage change in the peak amplitude of spine Ca^{2+} transients and Ca^{2+} spike amplitude (Pearson correlation). Data are mean \pm s.e.m. *** $P < 0.001$, paired *t*-test and Wilcoxon matched-pairs signed rank test. See Methods for statistical details.

synaptic plasticity. To investigate this further, we examined how the generation of branch-specific Ca^{2+} spikes is regulated and whether its disruption affects synaptic plasticity induced by different learning experiences.

Several lines of evidence suggest that the generation of Ca^{2+} spikes is regulated by cortical inhibition^{27,28}. We found that local application of GABA_A receptor antagonist bicuculline in layer I (L1) did not increase Ca^{2+} spike number but increased the overlap index of spikes induced by FWR and BWR (Extended Data Fig. 8a, b). We further examined the effects of deleting or silencing somatostatin (SST)-expressing cortical interneurons, which form synapses with apical tuft dendrites of L5 pyramidal neurons^{29,30}. SST-interneuron deletion was accomplished with *SST-IRES-Cre/Rosa26-LSL-iDTR* mice in which diphtheria toxin treatment activated diphtheria toxin receptors (DTR)³¹ and led to a specific loss ($69 \pm 4\%$) of SST neurons over 2 days (Fig. 4a and Extended Data Fig. 8c, d; before deletion: 877 cells; after deletion: 222 cells; $n = 5$ mice). SST-interneuron silencing was achieved with the designer receptors exclusively activated by designer drugs (DREADD) approach³² in which activation of $G_{i/o}$ -coupled human muscarinic M4 designer receptor by clozapine-*N*-oxide (CNO) induced a significant reduction in somatic Ca^{2+} activity of SST interneurons *in vivo* (Fig. 4b and Extended Data Fig. 8e; $P = 0.0001$; 27 somata; $n = 4$ mice). We found that either deletion or silencing of SST neurons caused loss of branch specificity of Ca^{2+} spikes without affecting the total number of Ca^{2+} spikes induced during running (Fig. 4c–e and Extended Data Fig. 8f; overlap index in control mice: $<10\%$; overlap index in SST-deleted or silenced mice: $\sim 40\%$). Thus, inactivating SST-interneurons disrupts branch-specific generation of Ca^{2+} spikes when mice perform different motor running tasks.

To test whether loss of branch-specificity of Ca^{2+} spikes affects the maintenance of synaptic plasticity, we first identified spines potentiated by Ca^{2+} spikes during FWR and then examined these potentiated spines during BWR in both SST-intact control and SST-deleted mice (Fig. 4f). Similar to control mice, the initial FWR session in SST-deleted mice induced potentiation ($82.6 \pm 8.8\%$) of Ca^{2+} transients in spines active at the time of spike generation (Extended Data Fig. 8g, h; $P < 0.001$; $n = 49$). Notably, during BWR, a larger fraction of FWR-potentiated

spines underwent depotentiation in SST-deleted mice when compared to control mice (Fig. 4g; spines showing reduced $\Delta F/F_0$ after BWR training: 24 out of 34 (SST-deleted) and 8 out of 18 (SST-intact)). Detailed analyses show that many of these depotentiated spines were active within 5 s before Ca^{2+} spikes induced by BWR in SST-deleted mice (Fig. 4g, h). Owing to the loss of branch-specific generation of Ca^{2+} spikes, FWR-potentiated spines were depotentiated more often in SST-deleted mice than in control mice because they were more likely to be on the same dendrites in which BWR-induced Ca^{2+} spikes occurred.

In addition to being depotentiated, a fraction of FWR-potentiated spines were active during Ca^{2+} spikes induced by BWR and underwent further potentiation in SST-deleted mice (Fig. 4g, h). However, more spines were depotentiated than potentiated after BWR. Consequently, when BWR followed FWR, there was a net depotentiation of Ca^{2+} transients in FWR-potentiated spines in SST-deleted mice (Fig. 4i; $P < 0.05$; $n = 34$). In control mice, no such net depotentiation was observed ($P = 0.32$). Moreover, when the initial FWR was followed by a second FWR session, previously potentiated spines showed no net depotentiation in control mice and further net potentiation in SST-deleted mice (Fig. 4i; control: $P = 0.15$; SST-deleted: $P < 0.05$). Together, these findings indicate that the loss of branch-specific generation of Ca^{2+} spikes reduces synaptic potentiation induced by one task when a different task is learned.

Disrupting BSDCS causes learning interference

The functional consequences of disrupting branch-specific Ca^{2+} spikes and synaptic plasticity at apical tuft branches remain unclear. We found that local application of tetrodotoxin (TTX) to L1, but not L5, significantly reduced the number of tuft Ca^{2+} spikes as well as Ca^{2+} transients in the apical trunk nexus in mice running on the treadmill (Fig. 5a, b; $P < 0.001$). TTX application to L1 also reduced Ca^{2+} activity in L5 neuronal somata (Fig. 5c and Extended Data Fig. 9a–c). These observations are consistent with previous studies showing that synaptic inputs and Ca^{2+} spikes on tuft branches have a profound effect on the output of L5 pyramidal neurons by causing the depolarization in apical trunks and somata^{33–35} (Extended Data Fig. 4 and Supplementary Information).

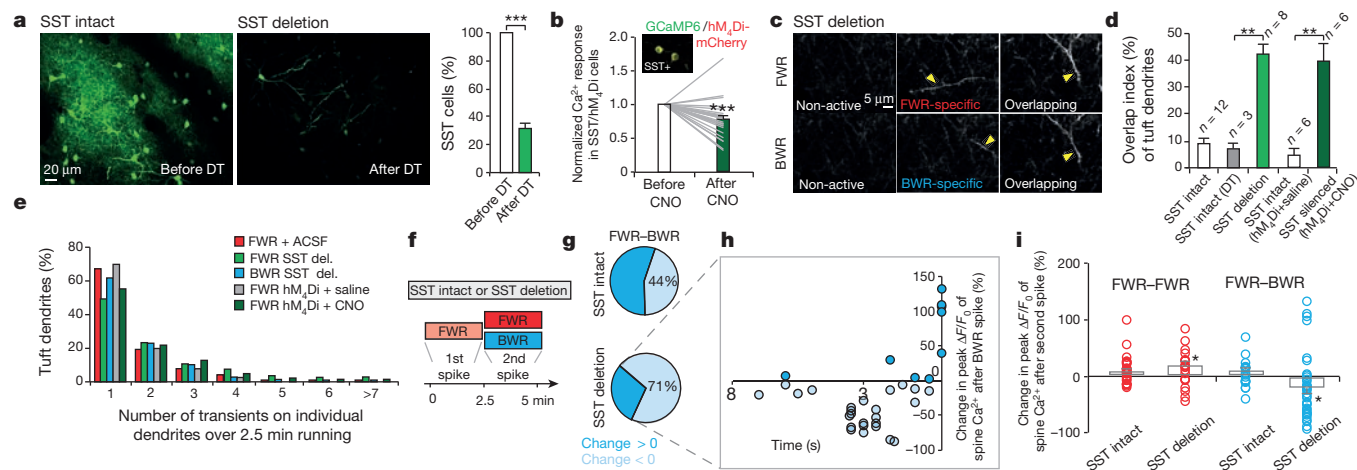


Figure 4 | Disrupting cortical inhibition alters branch-specific Ca^{2+} spikes and synaptic potentiation. **a**, Two-photon images of SST-interneurons labelled with green fluorescent protein (GFP) in motor cortex before and 2 days after diphtheria toxin (DT) treatment. Loss of SST interneurons occurred within 2 days after diphtheria toxin treatment. **b**, Somatic Ca^{2+} activity was reduced after CNO in SST interneurons expressing hM4Di-mCherry/GCaMP6s (inset). **c**, Two-photon images of tuft dendrites exhibiting spikes during FWR and BWR after SST deletion. **d**, SST deletion or silencing significantly increased the percentage of tuft dendrites exhibiting Ca^{2+} spikes during both FWR and BWR (SST/DTR: $P = 0.0007$; SST/hM4Di: $P = 0.002$). **e**, Inactivating SST interneurons did not affect the number of Ca^{2+} spikes

generated during FWR as compared to control mice ($P > 0.05$). More than 200 Ca^{2+} spikes were measured per condition. del., deletion. **f**, Training protocol to test the effect of disrupting branch-specific Ca^{2+} spikes on potentiated spine Ca^{2+} transients in control and SST-deleted mice. **g**, Pie charts showing 44% and 71% of FWR-potentiated spines were depotentiated during BWR in control and SST-deleted mice, respectively. **h**, Spines potentiated during FWR were depotentiated when active < 5 s before BWR-induced Ca^{2+} spikes in SST-deleted mice. **i**, Summary of the effect of FWR or BWR on previously potentiated spines in control and SST-deleted mice. Data are mean \pm s.e.m. $*P < 0.05$, $**P < 0.01$, $***P < 0.001$, paired *t*-test (**a**, **d**, **i**) and Wilcoxon matched-pairs signed rank test (**b**, **i**). Statistical details in Methods.

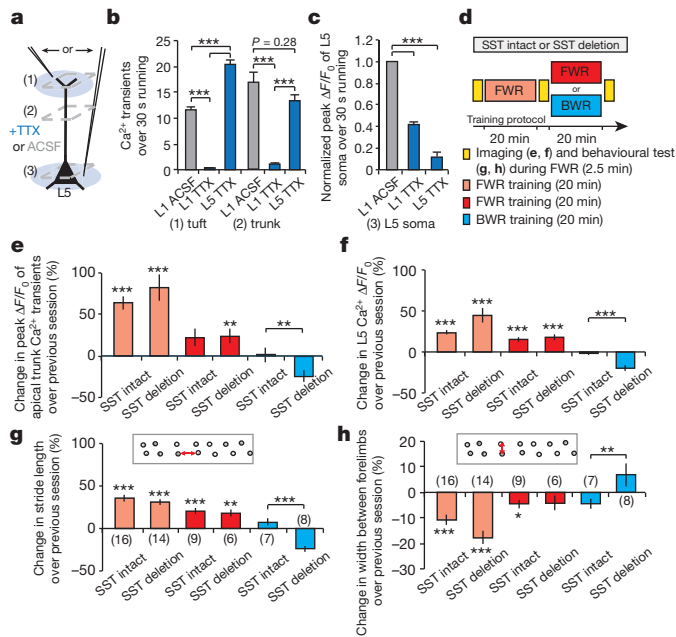


Figure 5 | Deletion of SST-interneurons impairs soma activities of L5 pyramidal neurons and performance improvement after learning. **a–c**, TTX applied to L1, but not L5, inhibited Ca^{2+} spike generation in the apical tuft and trunk. TTX to L1 also reduced Ca^{2+} transients in L5 somata during FWR. **d**, Experimental design to assess the effect of disrupting branch-specific Ca^{2+} spike on activities of apical trunks and somata, as well as behavioural performance in SST-deleted mice. **e, f**, In control and SST-deleted mice, Ca^{2+} activity at the trunk nexus (control: $n = 64$; deleted: $n = 61$) and L5 soma (control: $n = 113$; deleted: $n = 74$) increased after an initial and second sessions of FWR. BWR after the initial FWR significantly reduced Ca^{2+} activity at trunk (control: $n = 107$; deleted: $n = 77$) and L5 somata (control: $n = 63$; deleted: $n = 67$) in SST-deleted mice when compared to control mice. **g, h**, When FWR was followed by BWR, SST-deleted mice, but not control mice, displayed a reduction of the stride length and an increase in the width between forelimbs when tested in FWR. Number of mice per group is indicated. Data are mean \pm s.e.m. * $P < 0.05$, ** $P < 0.01$, *** $P < 0.001$, Mann–Whitney U test (**b–f**) and paired t -test (**g, h**). See Methods for statistical details.

To test the functional effect of disrupting branch-specific Ca^{2+} spikes, we compared Ca^{2+} activities in apical trunks and L5 somata in control and SST-deleted mice subjected to FWR and/or BWR (Fig. 5d). In both control and SST-deleted mice, there was a substantial increase of Ca^{2+} activity in the trunk nexus and L5 somata during the first (0–20 min) and second (20–40 min) FWR training session (Fig. 5d–f). This increase of Ca^{2+} transients in trunks was blocked by local application of CaMKII inhibitors to L1 (Extended Data Fig. 9d, e). When the initial FWR was followed by BWR, there was no significant change in Ca^{2+} transients that were potentiated in the trunks and somata during the initial FWR session in control mice (Fig. 5d–f; change from 20–40 min: $1.0 \pm 9.2\%$ (trunk), $P = 0.12$; $-1.0 \pm 1.6\%$ (L5 soma), $P = 0.10$). By contrast, in SST-deleted mice, there was a significant reduction in previously potentiated Ca^{2+} transients in both trunks and somata (Fig. 5d–f; change from 20–40 min: $-24.2 \pm 7.1\%$ (trunk), $P < 0.001$; $-19.8 \pm 3.3\%$ (L5 soma), $P < 0.001$). Together, these experiments indicate that in SST-deleted mice, a new learning task not only interferes with the maintenance of synaptic potentiation (Fig. 4) but also causes a reduction in the soma activities of L5 pyramidal neurons that are potentiated during a previously learned task.

When motor performance (stride length and width between forelimbs in steady FWR) was measured (Fig. 5d), control mice showed performance improvements when trained to FWR or BWR after the initial FWR (Fig. 5d, g, h). Similar to control mice, SST-deleted mice showed a progressive increase in the stride length and a decrease in the width between forelimbs when only running forward (Fig. 5d, g, h and

Supplementary Information). However, when mice were subjected to BWR after FWR and their performances in FWR were tested again, SST-deleted mice exhibited a significant reduction in the stride length and an increase in the width between forelimbs when compared to control mice (Fig. 5d, g, h; $P < 0.001$ (length); $P < 0.01$ (width)). Additionally, when mice were subjected to motor learning on an accelerated rotarod³⁶, SST-deleted mice, but not the control mice, showed a significant reduction in FWR performance after BWR (Extended Data Fig. 10a). Together, these results suggest that disrupting branch-specific Ca^{2+} spikes and synaptic potentiation on apical tuft dendrites interferes with increased activities of L5 pyramidal neurons and behavioural improvement when multiple motor tasks are learned.

Discussion

How neural circuits encode and store vast amounts of information without significant interferences remains unclear. By performing Ca^{2+} imaging in the motor cortex of awake, behaving mice, we show that different motor learning experiences trigger NMDA-receptor-dependent Ca^{2+} spikes in non-overlapping apical tuft branches of L5 pyramidal neurons. This spatial segregation of Ca^{2+} spikes is crucial for the induction and maintenance of synaptic plasticity when several tasks are learned (Extended Data Fig. 10b). These findings indicate that dendritic-branch-specific generation of Ca^{2+} spikes is a fundamental mechanism used in the brain to store different information with little or no interference.

Our studies in the motor cortex are consistent with a view that individual dendritic branches serve as a basic unit for synaptic plasticity and information storage^{37–40}. Recent studies have shown that NMDA-receptor-dependent Ca^{2+} spikes are involved in input integration and amplification in sensory cortices and hippocampus^{15–19}. As in the motor cortex, NMDA-receptor-dependent Ca^{2+} spikes in these brain regions may also have an important role in experience-dependent synaptic plasticity. Unlike the motor cortex, however, Ca^{2+} spikes in the barrel cortex occur in all apical tuft branches of an individual L5 pyramidal neuron¹⁵. It would be interesting to investigate whether the lack of branch-specific generation of Ca^{2+} spikes in sensory cortices might compromise the maintenance of experience-dependent synaptic plasticity during sensory processing and perceptual learning. Furthermore, in addition to SST-expressing interneurons, the generation of branch-specific Ca^{2+} spikes and their effect on synaptic plasticity are probably regulated by other types of inhibitory neurons, ion channels and behavioural context^{5,13,41–43}. Future studies are needed to investigate these issues to understand better how information is encoded and stored in the brain.

Online Content Methods, along with any additional Extended Data display items and Source Data, are available in the online version of the paper; references unique to these sections appear only in the online paper.

Received 10 June 2014; accepted 21 January 2015.

Published online 30 March 2015.

- Martin, S. J., Grimwood, P. D. & Morris, R. G. Synaptic plasticity and memory: an evaluation of the hypothesis. *Annu. Rev. Neurosci.* **23**, 649–711 (2000).
- Neves, G., Cooke, S. F. & Bliss, T. V. Synaptic plasticity, memory and the hippocampus: a neural network approach to causality. *Nature Rev. Neurosci.* **9**, 65–75 (2008).
- Abraham, W. C. & Robins, A. Memory retention—the synaptic stability versus plasticity dilemma. *Trends Neurosci.* **28**, 73–78 (2005).
- Ross, W. N. & Werman, R. Mapping calcium transients in the dendrites of Purkinje cells from the guinea-pig cerebellum *in vitro*. *J. Physiol. (Lond.)* **389**, 319–336 (1987).
- Jaffe, D. B. *et al.* The spread of Na^+ spikes determines the pattern of dendritic Ca^{2+} entry into hippocampal neurons. *Nature* **357**, 244–246 (1992).
- Schiller, J., Schiller, Y., Stuart, G. & Sakmann, B. Calcium action potentials restricted to distal apical dendrites of rat neocortical pyramidal neurons. *J. Physiol. (Lond.)* **505**, 605–616 (1997).
- Spruston, N. Pyramidal neurons: dendritic structure and synaptic integration. *Nature Rev. Neurosci.* **9**, 206–221 (2008).
- Major, G., Larkum, M. E. & Schiller, J. Active properties of neocortical pyramidal neuron dendrites. *Annu. Rev. Neurosci.* **36**, 1–24 (2013).
- Golding, N. L., Staff, N. P. & Spruston, N. Dendritic spikes as a mechanism for cooperative long-term potentiation. *Nature* **418**, 326–331 (2002).

10. Kampa, B. M., Letzkus, J. J. & Stuart, G. J. Requirement of dendritic calcium spikes for induction of spike-timing-dependent synaptic plasticity. *J. Physiol. (Lond.)* **574**, 283–290 (2006).
11. Remy, S. & Spruston, N. Dendritic spikes induce single-burst long-term potentiation. *Proc. Natl Acad. Sci. USA* **104**, 17192–17197 (2007).
12. Holthoff, K., Kovalchuk, Y., Yuste, R. & Konnerth, A. Single-shock LTD by local dendritic spikes in pyramidal neurons of mouse visual cortex. *J. Physiol. (Lond.)* **560**, 27–36 (2004).
13. Humeau, Y. & Luthi, A. Dendritic calcium spikes induce bi-directional synaptic plasticity in the lateral amygdala. *Neuropharmacology* **52**, 234–243 (2007).
14. Nevian, T. & Sakmann, B. Single spine Ca^{2+} signals evoked by coincident EPSPs and backpropagating action potentials in spiny stellate cells of layer 4 in the juvenile rat somatosensory barrel cortex. *J. Neurosci.* **24**, 1689–1699 (2004).
15. Xu, N. L. *et al.* Nonlinear dendritic integration of sensory and motor input during an active sensing task. *Nature* **492**, 247–251 (2012).
16. Lavzin, M., Rapoport, S., Polsky, A., Garion, L. & Schiller, J. Nonlinear dendritic processing determines angular tuning of barrel cortex neurons *in vivo*. *Nature* **490**, 397–401 (2012).
17. Smith, S. L., Smith, I. T., Branco, T. & Häusser, M. Dendritic spikes enhance stimulus selectivity in cortical neurons *in vivo*. *Nature* **503**, 115–120 (2013).
18. Grienberger, C., Chen, X. & Konnerth, A. NMDA receptor-dependent multidendritic Ca^{2+} spikes required for hippocampal burst firing *in vivo*. *Neuron* **81**, 1274–1281 (2014).
19. Palmer, L. M. *et al.* NMDA spikes enhance action potential generation during sensory input. *Nature Neurosci.* **17**, 383–390 (2014).
20. Yang, G. *et al.* Sleep promotes branch-specific formation of dendritic spines after learning. *Science* **344**, 1173–1178 (2014).
21. Marvin, J. S. *et al.* An optimized fluorescent probe for visualizing glutamate neurotransmission. *Nature Methods* **10**, 162–170 (2013).
22. Chen, T. W. *et al.* Ultrasensitive fluorescent proteins for imaging neuronal activity. *Nature* **499**, 295–300 (2013).
23. Harris, K. M. & Stevens, J. K. Dendritic spines of CA 1 pyramidal cells in the rat hippocampus: serial electron microscopy with reference to their biophysical characteristics. *J. Neurosci.* **9**, 2982–2997 (1989).
24. Matsuzaki, M. *et al.* Dendritic spine geometry is critical for AMPA receptor expression in hippocampal CA1 pyramidal neurons. *Nature Neurosci.* **4**, 1086–1092 (2001).
25. Sjöström, P. J. & Nelson, S. B. Spike timing, calcium signals and synaptic plasticity. *Curr. Opin. Neurobiol.* **12**, 305–314 (2002).
26. Lisman, J. & Spruston, N. Postsynaptic depolarization requirements for LTP and LTD: a critique of spike timing-dependent plasticity. *Nature Neurosci.* **8**, 839–841 (2005).
27. Murayama, M. *et al.* Dendritic encoding of sensory stimuli controlled by deep cortical interneurons. *Nature* **457**, 1137–1141 (2009).
28. Jiang, X., Wang, G., Lee, A. J., Stornetta, R. L. & Zhu, J. J. The organization of two new cortical interneuronal circuits. *Nature Neurosci.* **16**, 210–218 (2013).
29. Gentet, L. J. *et al.* Unique functional properties of somatostatin-expressing GABAergic neurons in mouse barrel cortex. *Nature Neurosci.* **15**, 607–612 (2012).
30. Chiu, C. Q. *et al.* Compartmentalization of GABAergic inhibition by dendritic spines. *Science* **340**, 759–762 (2013).
31. Saito, M. *et al.* Diphtheria toxin receptor-mediated conditional and targeted cell ablation in transgenic mice. *Nature Biotechnol.* **19**, 746–750 (2001).
32. Armbruster, B. N., Li, X., Pausch, M. H., Herlitze, S. & Roth, B. L. Evolving the lock to fit the key to create a family of G protein-coupled receptors potentially activated by an inert ligand. *Proc. Natl Acad. Sci. USA* **104**, 5163–5168 (2007).
33. Larkum, M. E., Nevian, T., Sandler, M., Polsky, A. & Schiller, J. Synaptic integration in tuft dendrites of layer 5 pyramidal neurons: a new unifying principle. *Science* **325**, 756–760 (2009).
34. Harnett, M. T., Xu, N. L., Magee, J. C. & Williams, S. R. Potassium channels control the interaction between active dendritic integration compartments in layer 5 cortical pyramidal neurons. *Neuron* **79**, 516–529 (2013).
35. Yuste, R., Gutnick, M. J., Saar, D., Delaney, K. R. & Tank, D. W. Ca^{2+} accumulations in dendrites of neocortical pyramidal neurons: an apical band and evidence for two functional compartments. *Neuron* **13**, 23–43 (1994).
36. Buitrago, M. M., Schulz, J. B., Dichgans, J. & Luft, A. R. Short and long-term motor skill learning in an accelerated rotarod training paradigm. *Neurobiol. Learn. Mem.* **81**, 211–216 (2004).
37. Losonczy, A., Makara, J. K. & Magee, J. C. Compartmentalized dendritic plasticity and input feature storage in neurons. *Nature* **452**, 436–441 (2008).
38. Polsky, A., Mel, B. W. & Schiller, J. Computational subunits in thin dendrites of pyramidal cells. *Nature Neurosci.* **7**, 621–627 (2004).
39. Govindarajan, A., Israely, I., Huang, S. Y. & Tonegawa, S. The dendritic branch is the preferred integrative unit for protein synthesis-dependent LTP. *Neuron* **69**, 132–146 (2011).
40. Euler, T., Detwiler, P. B. & Denk, W. Directionally selective calcium signals in dendrites of starburst amacrine cells. *Nature* **418**, 845–852 (2002).
41. Lee, S., Kruglikov, I., Huang, Z. J., Fishell, G. & Rudy, B. A disinhibitory circuit mediates motor integration in the somatosensory cortex. *Nature Neurosci.* **16**, 1662–1670 (2013).
42. Magee, J., Hoffman, D., Colbert, C. & Johnston, D. Electrical and calcium signaling in dendrites of hippocampal pyramidal neurons. *Annu. Rev. Physiol.* **60**, 327–346 (1998).
43. Ahissar, E. *et al.* Dependence of cortical plasticity on correlated activity of single neurons and on behavioral context. *Science* **257**, 1412–1415 (1992).

Supplementary Information is available in the online version of the paper.

Acknowledgements This work was supported by National Institutes of Health R01 NS047325 and P01 NS074972 to W.-B.G. We thank L. Looger, G. Chen and members of the Gan laboratory for their comments on the manuscript. We thank the Genetically-Encoded Neuronal Indicator and Effector (GENIE) Project and the Janelia Farm Research Campus of the Howard Hughes Medical Institute for sharing GCaMP6 constructs.

Author Contributions J.C. and W.-B.G. designed the experiments. J.C. performed experiments and analysed the data with the help from W.-B.G. J.C. and W.-B.G. prepared the manuscript.

Author Information Reprints and permissions information is available at www.nature.com/reprints. The authors declare no competing financial interests. Readers are welcome to comment on the online version of the paper. Correspondence and requests for materials should be addressed to W.-B.G. (gan@saturn.med.nyu.edu).

METHODS

Transgenic mice expressing GCaMP2.2c in L5 pyramidal neurons, *Thy1*-GCaMP2.2c (ref. 44), were received from G. Feng. Adeno-associated virus (AAV) experiments were conducted with C57/BL6 mice (Charles River Laboratory) and *Thy1*-Cre transgenic mice (FVB/N-Tg(*Thy1*-Cre)1Vln/J; the Jackson Laboratories), *SST-IRE5-Cre* mice (*Sst*^{tm2.1(cre)Zjh/J}) and *Rosa26-stop-iDTR* mice were purchased from the Jackson Laboratories. Mice were housed in the Parasitology Central Animal Facility at New York University Medical Center. All of the 1–1.5-month-old male and female animals were used for the experiments in accordance with the Institutional Guidelines.

Treadmill training and behavioural analysis. A custom-built free-floating treadmill (96 × 56 × 61 cm dimensions) was used for motor training in this study^{20,21}. This free-floating treadmill allows head-fixed mice to move their forelimbs freely to perform motor running tasks (forward, backward, left or right running). To minimize motion artefacts during imaging, the treadmill was constructed so that all the moving parts (motor, belt and drive shaft) have no contact with the microscope stage and the supporting air table. Animals were positioned on a custom-made head holder device that allowed the micro-metal bars (attached to the animal's skull) to be mounted and for the base of the device to be positioned below the belt in contact with the microscope stage. During motor training, the treadmill motor (Dayton, Model 2L010) was driven by a DC power supply (Extech). At the onset of a trial, the motor was turned on and the belt speed gradually increased from 0 cm s⁻¹ to 8 cm s⁻¹ within ~3 s.

Each running trial lasted 30 s. After completion of each trial, the treadmill was turned off and the next trial started after 30 s rest period. A backward running was introduced to provide mice with new motor learning experience. In this model, animals were forced to run backward on the treadmill (speed increased gradually from 0 to 4 cm s⁻¹ within ~3 s) for 30 s with the reversal of the treadmill motor. Left and right direction running was performed by shifting the custom-built head-holder device by 90° on the platform of the microscope, such that the mouse's limbs were perpendicular to the treadmill's belt. Turning on the treadmill caused the forelimbs of the head-restrained animal to move laterally. Mice completed five trials for each task, regardless of two task or four tasks running.

In Fig. 3, mice underwent a task-switching model in which mice were running forward, backward and then forward, all within a single trial (30 s for each direction, total running time 90 s). The task switching was accomplished quickly (within 1 s) by changing the polarity of the voltage applied to the motor. The belt speed was at 8 cm s⁻¹ throughout the forward and backward running sessions.

To assay running gait patterns, mouse forelimbs were coated in ink (Speedball) before each running trial and white paper (45-cm long) was taped to the belt. Mice ran on white paper over five trials (30 s each) with 30 s inter-trial interval. The stride length and the width between forelimbs were analysed over the first 10 s of each 30 s trial. Footprints were analysed offline manually by three measures: (1) the fraction of time spent in gait pattern over five trials (four groups: drag, sweep, wobble and steady run); (2) the stride length between two ipsilateral forelimb footprints in steady run gait pattern; and (3) the width between two forelimbs. The stride length and the width between forelimbs were averaged over five trials per animal before and after two 20-min training epochs. In early forward running trials, mice exhibited various gait patterns including drag (35%), sweep (15%), wobble (30%) and steady run (20%), and with continued training, mice refined their gait patterns from drag (13%), sweep (12%) and wobble (29%) into steady run (46%) (Fig. 1b and Extended Data Fig. 1). We define drag as a gait pattern in which mice failed to execute steps, which resulted in a smearing of ink during the trial run. Sweep occurs as mice make distinct, yet lateral forelimb steps resulting ink marks perpendicular to the direction of running. Wobble occurs when mice make many disorganized, chaotic steps resulting in an ink pattern that appears highly variable in and lateral to the running direction. During steady run, mice make distinct steps resulting in spaced ink marks centred in the direction of the running trial. As shown in Fig. 1 and Extended Data Fig. 1, we observed changes in the stride length and the width between forelimbs when mice achieved steady run gait over forward training. Similar to forward running, backward running also elicited changes in gait patterns and the stride length over 40-min training (see Extended Data Fig. 1). The primary motor cortex is necessary for this task as local pharmacological inactivation with muscimol prevented the emergence of steady run gait patterning (Extended Data Fig. 1e).

Rotarod training and behavioural analysis. An EZRod system with a test chamber (44.5 × 14 × 51 cm, Accuscan Instruments) was used as another motor training model different from treadmill running²⁰. Animals were placed on the motorized rod (30 mm in diameter) in the chamber. The rotation speed gradually increased from 0 to 100 r.p.m. over the course of 3 min. The time latency and rotation speed were recorded when the animal was unable to keep up with the increasing speed and fell from the rod. Rotarod training was performed in two training sessions each consisting of 20 trials. Rotarod performance was tested in five trials before the

training as well as after the first and second training session. Performance was measured as the average speed animals achieved during the five trials at each time point. To test motor interference, backward running was introduced after the first forward running session. In this regime, animals were subjected to run backward on the rotating rod (speed increased gradually from 0 to 40 r.p.m. over 3 min) for 20 trials. After backward running, animals were tested for their forward running performance (Extended Data Fig. 10a).

Surgical preparation for imaging awake, head-restrained mice. Dendritic imaging was carried out in awake, head-restrained mice through a thinned-skull window. Surgery preparation for awake animal imaging includes attaching the head holder and creating a thinned-skull cranial window⁴⁵. Specifically, mice were deeply anaesthetized with an intraperitoneal injection of ketamine (100 µg g⁻¹) and xylazine (10 µg g⁻¹). The mouse head was shaved and the skull surface was exposed with a midline scalp incision. The periosteum tissue over the skull surface was removed without damaging the temporal and occipital muscles.

A head holder composed of two parallel micro-metal bars was attached to the animal's skull to help restrain the animal's head and reduce motion-induced artefact during imaging. A small skull region (~0.2 mm in diameter) was located over the primary motor cortex based on stereotactic coordinates (at bregma and 1.2 mm lateral from the midline) and marked with a pencil⁴⁶. A thin layer of cyanoacrylate-based glue was first applied to the top of the entire skull surface, and the head holder was then mounted on top of the skull with dental acrylic cement (Lang Dental Manufacturing Co.) such that the marked skull region was exposed between the two bars. Precaution was taken not to cover the marked region with dental acrylic cement.

After the dental cement was completely dry, the head holder was screwed to two metal cubes that were attached to a solid metal base, and a cranial window was created over the previously marked region. The procedures for preparing a thinned skull cranial window for two-photon imaging have been described in detail previously⁴⁵. In brief, a high-speed drill was used to reduce carefully the skull thickness by approximately 50% under a dissecting microscope. The skull was immersed in artificial cerebrospinal fluid (ACSF) during drilling. Skull thinning was completed by carefully scraping the cranial surface with a microsurgical blade to ~20 µm in thickness. A high quality picture of the brain vasculature was taken with a CCD camera attached to a stereo dissecting microscope. The completed cranial window was covered with silicone elastomer (World Precision Instruments) and the animals were returned to their own cages to recover. For calcium imaging of L5 somata, a small piece of bone overlying the primary motor cortex was removed, and a round glass coverslip (approximately the same size as the bone being removed) was glued to the skull to reduce motion of the exposed brain.

Imaging experiments were started ~12–24 h after window implantation. After awakening, mice with head mounts were habituated for a few times (10 min each time) in the treadmill-adapted imaging apparatus to minimize potential stress effects of head restraining, motor training and imaging. Awake mice were head restrained in the imaging apparatus, which sits on top of a custom-built free-floating treadmill.

Two-photon calcium imaging of dendrites and somata of L5 neurons expressing GCaMPs. Genetically encoded calcium indicators including GCaMP6s, GCaMP5G, GCaMP3 and GCaMP2.2c were used for Ca²⁺ imaging of dendritic spikes of L5 pyramidal neurons in the primary motor cortex (a region ~200 µm in square and centred at ~0.5 mm anterior from bregma and ~1.2 mm lateral from the midline). GCaMPs were expressed with recombinant AAV under the human synapsin-1 (*SYN1*) promoter (AAV, serotype 2/1; >2 × 10¹³ genome copies per ml; produced by the University of Pennsylvania Gene Therapy Program Vector Core). A total of 0.1–0.2 µl of AAV viruses was diluted 10 times in ACSF and slowly injected (Picospritzer III; 15 p.s.i., 12 ms, 0.8 Hz) over 10–15 min into L5 (depth of 500–700 µm) of primary motor cortex using a glass microelectrode around the coordinate of 0.5 cm anterior and 1.5 cm lateral from bregma⁴⁶. The ACSF dilution allowed better spread of viruses through L5 and sparse neuronal labelling. Sparse expression of GCaMP ensures that the contribution of fluorescent signals from the neuropil to the dendrites and somata is negligible. In addition to *SYN1*-driven GCaMPs, *Thy1*-Cre transgenic mice (FVB/N-Tg(*Thy1*-Cre)1Vln/J; Jackson stock number: 6143) were used in combination with Cre-dependent AAV-CAG-Flex-GCaMP6s. In these mice, Cre is exclusively expressed in pyramidal neurons. For double labelling of GCaMP6 and a structural marker (tdTomato), two viruses (AAV2/1-CAG-Flex-GCaMP6s and AAV2/1-CAG-Flex-tdTomato; serotypes 2/1; >2 × 10¹³ genome copies per ml) were mixed at equal volumes and injected into L5 of the motor cortex. In experiments where L5 soma calcium activity was imaged, *Thy1*-Cre transgenic mice were used to label L5 pyramidal neurons specifically⁴⁴.

Motor cortex containing GCaMP-positive apical dendritic branches (from L5 neurons) at the depth of 0–200 µm below the pial surface were imaged for detecting the activities of tuft dendrites. In mice infected with viruses, to confirm that layer 2/3 were not labelled by GCaMP6, a glass window was placed over the region

of interest following the completion of imaging experiments, and imaging of layer 2/3 was performed to ensure the absence of GCaMP6 expression in layer 2/3 neurons.

In vivo two-photon imaging was performed with an Olympus Fluoview 1000 two-photon system (tuned to 920 nm) equipped with a Ti:Sapphire laser (MaiTai DeepSee, Spectra Physics). The average laser power on the tissue sample was ~20–30 and 50–60 mW for imaging in the L1 and L5 of the cortex respectively. All experiments were performed using a $\times 25$ objective (numerical aperture 1.1) immersed in an ACSF solution and with a $\times 1.5$ (soma) and $\times 4$ (dendrites) digital zoom. All images were acquired at frame rates of 2 Hz (2- μ s pixel dwell time) except for Fig. 1e and Extended Data Fig. 2d–f in which images were acquired at 4 Hz. Typical imaging window for Ca^{2+} imaging of tuft dendrites was 160 μm by 80 μm . Image acquisition was performed using FV10-ASW v.2.0 software and analysed post hoc using NIH ImageJ software.

Two-photon laser cutting of tuft dendrites of L5 pyramidal neurons. In Extended Data Fig. 4, dendrites expressing GCaMPs were cut by parking the two-photon laser beam on a small ROI that spanned the diameter of the dendrite for 5 s (tuned to ~890 nm and power was increased gradually until a sudden increase in fluorescence intensity was observed). After laser cut, a physical break could be observed between the two segments of dendrite. In the control experiment, the laser beam was parked ~30 μm away from the branch of interest without damaging it (Extended Data Fig. 4e).

Drugs applications. Approximately 200 μl of MK801 (M107, Sigma Aldrich), bicuculline (C2503, Tocris Bioscience), CaMKII inhibitors KN-93 (K1385, Sigma Aldrich)/KN-62 (I2142, Sigma Aldrich) or TTX citrate (1069; Tocris) was applied with a pipette to the surface of the primary motor cortex after removing a small bone flap (~200 μm in diameter) adjacent to a thinned skull window. CaMKII inhibitors KN-62 (100 μM) and KN-93 (100 μM) were first dissolved in dimethylsulphoxide (DMSO) and then in ACSF. The final DMSO concentration is lower than 1% (v/v) in ACSF. MK801 (100 μM), bicuculline (100 μM) and TTX (100 μM) were dissolved directly in ACSF to final concentrations. The bone flap for drug delivery was made during awake head mounting and covered with a silicone elastomer such that it could be easily removed at the time of imaging. Because small molecules diffuse rapidly in the cortex, we estimated that the drug concentration was reduced ~10 times in the imaged cortical region, such that the final effective concentration for CaMKII inhibitors, MK801, bicuculline and DMSO would be 10 μM , 10 μM and <0.1%, respectively. As the control experiment, we applied ACSF after removing a bone flap.

In experiments in which TTX and ACSF were injected to L1 and 5, we used a similar approach to that of virus injections (see above). In brief, TTX or ACSF was slowly injected to L1 or 5 (1 μl of 10 μM TTX in ACSF) with a glass microelectrode via pressure injections (Picospritzer III; 15 p.s.i., 12 ms, 0.8 Hz) 0.5 mm lateral to the forelimb motor region at a depth of 500–700 μm below the pial surface (Fig. 5a and Extended Data Fig. 9a, b). Mice were allowed to awake from weak isoflurane anaesthesia over the next 20 min. Ca^{2+} imaging was performed 20 min after TTX injection in L1 or L5 in the forelimb region of the motor cortex. To map the extent of local TTX diffusion, Texas Red dye was mixed and co-injected to the cortex. After imaging, mice were perfused with 4% paraformaldehyde (PFA) and their brains were postfixed overnight. Brains were sectioned with a vibratome at 100- μm sections. Confocal images were acquired using a Zeiss LSM 700 confocal microscope ($\times 10$ air objective, numerical aperture 0.3). The extent of Texas Red dye spread was estimated by the line at which the Texas Red fluorescence was less than 20% of its peak level. On the basis of this definition, we determined the fluorescence signals Texas Red spread to a region $237 \pm 19 \mu\text{m}$ in L5 and $188 \pm 10 \mu\text{m}$ in L1, respectively (Extended Data Fig. 9a, b).

Muscimol (Sigma) inactivation was achieved by thinning the skull overlying forelimb motor cortex and creating a small bone flap (~200 μm in diameter) where ~100 nl of muscimol (5 $\mu\text{g} \mu\text{l}^{-1}$ in ACSF) or ACSF (control injection in forelimb region) was injected bilaterally (Picospritzer III; 15 p.s.i., 12 ms, 0.8 Hz) over 10–15 min into the motor cortex at depth of ~500–700 μm from pial surface, under isoflurane anaesthesia. The bone flap was then sealed and mice were allowed to recover in their home cage for >1 h before treadmill training. For control injections in a region other than forelimb motor cortex, muscimol was injected in the barrel cortex, using the coordinate of 1.3 mm posterior and 3.5 mm lateral from bregma. **SST neuron deletion and silencing.** Deletion of SST interneurons was accomplished in *SST-IRES-Cre/Rosa26-stop-iDTR* mice by intraperitoneal injection of 1 μg diphtheria toxin (Sigma Aldrich) (three injections 12 h apart; diphtheria toxin diluted in saline; 1 μg diphtheria toxin/100 μl saline). *In vivo* two-photon imaging was performed to examine the loss of layer 2/3 SST interneurons in *SST-IRES-Cre/Rosa26-stop-iDTR* mice infected with AAV-CAG-Flex-GFP viruses before and 2 days after diphtheria toxin treatment. Deletion efficiency over two days was calculated by counting the number of SST GFP-positive somata in the same region of the forelimb motor cortex (from the pial surface to layer 2/3 (depth of approximately 250 μm)) in a 0.03 mm² cortical window) before and after diphtheria toxin treatment.

To examine the specificity of SST deletion and its effect on other cortical cells in motor cortex, we examined parvalbumin interneurons and microglia (Iba1) cell density by immunohistochemistry following 2 days after SST deletion. After imaging experiments, mice were anaesthetized and perfused with 20 ml PBS. The brain was removed and fixed for 1 h in 4% PFA at 4 °C. Tissue was rinsed three times with PBS, embedded in 2% agarose, and sectioned at 100 μm with a vibratome. Sections were permeabilized in 1% Triton X-100 in PBS for 3 h and blocked with 5% normal goat serum for 1 h. Sections were incubated overnight with primary antibodies against parvalbumin (Sigma, 1:300) and Iba1 (Wako, 1:500). Sections were then washed three times with PBS/0.05% Tween-20, and then incubated with Alexa Fluor-conjugated goat anti-rabbit IgG secondary antibodies (Life Technologies) 1:500 in PBS for 2 h. Sections were washed and mounted for imaging. Confocal images were obtained on a Zeiss LSM 700 confocal microscope. We found that there was no difference in the density (imaging area: parvalbumin, $1,250 \times 1,250 \mu\text{m}^2$; Iba1, $250 \times 250 \mu\text{m}^2$) of parvalbumin-positive cells or Iba1-positive microglia cells in forelimb motor cortex of mice deleted of SST cells as compared to control mice with SST cells ($P = 0.22$ and $P = 0.55$ for parvalbumin and Iba1 respectively; Extended Data Fig. 8c, d).

For acute SST interneuron silencing, Cre-dependent AAV2-hSyn-DIO-hM₄D(Gi)-mCherry was used to drive DREADD expression in *SST-IRES-Cre/Thy1-GCaMP2.2c* mice (AAV, serotype 2/1; ~10¹² genome copies per ml; produced by UNC Vector Core). For validation of DREADD-hM₄Di silencing of SST interneuron activity, two viruses (AAV2/1-CAG-Flex-GCaMP6s and AAV2-hSyn-DIO-hM₄Di-mCherry) were mixed at equal volumes and injected into primary motor cortex of *SST-IRES-Cre* mice. Viruses were injected into the primary motor cortex two weeks before Ca^{2+} imaging. CNO (C0832, Sigma Aldrich) was dissolved in saline to a concentration of 0.5 mg ml⁻¹. Ca^{2+} imaging of dendritic tufts was performed during the initial running trials (forward and backward) without CNO. Twenty minutes after CNO was administered by intraperitoneal injection to each mouse (0.3 ml per 30 g body weight), the same cortical region was re-imaged during a second session of running trials (Extended Data Fig. 8f).

It should be noted that the efficiency of CNO in activating hM₄Di was tested by expressing Flex-GCaMP6 and DIO-hM₄Di-mCherry in the same cell. We found that in SST neurons that were co-transfected with hM₄Di-mCherry and GCaMP6 viruses, the expression level of hM₄Di-mCherry was significantly lower than that in SST neurons transfected with hM₄Di-mCherry viruses only (Extended Data Fig. 8e). In the experiments in which dendritic Ca^{2+} spikes and the overlap index in pyramidal neurons were measured (Fig. 4c, d), SST neurons were transfected only with hM₄Di-mCherry viruses. We expect that the reduction of SST neuronal activity in those experiments would be higher (probably ~2-fold) than that shown in Fig. 4b.

Imaging data analysis. ROIs corresponding to visually identifiable spines, apical tuft dendrites or somata were selected for quantification. During running trials, the lateral movement of the images was typically less than 1 μm . Vertical movements were infrequent and minimized owing to flexible belt design, two micro-metal bars attached to the animal's skull (described above) by dental acrylic, and a custom-built body support to minimize spinal cord movements generated by the hindlimbs. All imaging stacks were registered using ImageJ plugin StackReg. Active spines, dendrites and L5 pyramidal neurons that could be identified in all imaged sessions were included in the data set. The fluorescence time course of each spine, dendritic segment or cell body was measured with ImageJ software by averaging all pixels within the ROIs covering the dendrite or somata. The $\Delta F/F_0$ value was calculated as $\Delta F/F_0 = (F - F_0)/F_0 \times 100\%$, in which F_0 is the baseline fluorescence signal averaged over a 2-s period before the onset of the motor task. In all imaging sessions, resting awake images were collected before running trials.

Dendritic Ca^{2+} spikes were defined as the events when changes of fluorescence ($\Delta F/F_0$) observed in both dendritic spines and shaft (or dendritic branch) were >35% for GCaMP6s and >20% for GCaMP2.2c during the 2.5-min imaging sessions. F_0 is the fluorescence intensity in dendritic segments after background subtraction. Fluorescence background was measured from a region adjacent to the dendrite segment. The threshold for detecting dendritic spikes was more than three times the standard deviation of baseline fluorescence noise for GCaMP6s or GCaMP2.2c, respectively. As shown in Fig. 1h, most Ca^{2+} spikes were found to have a fluorescence increase of 100 to >1,000% for GCaMP6s and 50 to >200% for GCaMP2.2c.

In Extended Data Fig. 2f, Ca^{2+} spike rise time was determined by measuring the time between the threshold of detecting dendritic spikes to the peak amplitude. Decay time was measured as the time between the peak amplitude and the decay back to the threshold. The Ca^{2+} spike frequency was determined by recording the number of Ca^{2+} spikes over 2.5 min from the same motor region under various conditions (Extended Data Fig. 2h).

In Fig. 1i, task-specific Ca^{2+} spikes were defined as dendrites that showed activity (one or more events) in one task but not in the other running task (a 2.5-min imaging

session for each direction). In Fig. 4d, the overlap index was calculated by dividing the number of Ca^{2+} spikes on individual dendrites that activated during both forward/backward running trials by the number of Ca^{2+} spikes detected on individual dendrites that activated during forward or backward or both running trials.

Dendritic spine Ca^{2+} transients are defined as those with changes of fluorescence ($\Delta F/F_0$) > 35% for GCaMP6s and > 15% for GCaMP2.2c during the 2.5-min imaging sessions. The threshold is more than three times the standard deviation of baseline fluorescence noise for GCaMP6s ($\Delta F/F_0$: $33.9 \pm 3.1\%$) and GCaMP 2.2c ($\Delta F/F_0$: $13.6 \pm 3.7\%$). Spine Ca^{2+} transients detected with GCaMP6s were found to have an average fluorescence increase of $100.2 \pm 3.8\%$ ($\Delta F/F_0$) with 52% of spines exhibiting 1–4 transients per 2.5 min and 48% of spines exhibiting > 5 transients per 2.5 min. In GCaMP2.2c-expressing dendrites, the average peak $\Delta F/F_0$ of Ca^{2+} transients in spines is $33 \pm 0.9\%$ during forward running trials. On average, active spines detected with 2.2c exhibited 3 transients per 2.5 min ($n = 65$ spines from 12 dendritic branches).

Ca^{2+} spikes and spine Ca^{2+} transients under analysis were always on the same branches. Consistent with previous studies²², the ratio of Ca^{2+} fluorescence intensity in spine heads to neighbouring shafts for inactive spines was 0.46 ± 0.02 for GCaMP6s and 0.41 ± 0.02 for GCaMP2.2c (Extended Data Fig. 5k, l). For spines active at the time of spike generation and analysed in the present study, this ratio was 1.56 ± 0.13 for GCaMP6s and 1.71 ± 0.10 for GCaMP2.2c, significantly higher than that for neighbouring inactive spines (Extended Data Fig. 5k, l; $P < 0.001$). In Fig. 2, Ca^{2+} spike-induced potentiation of spines was determined by measuring the percentage change of the average peak $\Delta F/F_0$ of transients before and after Ca^{2+} spike generation. Most spines undergoing Ca^{2+} spike-induced potentiation had several spine transients before and after the spike. In Fig. 2, the peak $\Delta F/F_0$ of 3–4 Ca^{2+} transients from each spine was averaged before and after the spike to measure Ca^{2+} spike-induced changes. For active spines that did not experience a Ca^{2+} spike, 3–4 transients per spine were analysed for peak $\Delta F/F_0$ and compared between the first two and last two running trials. In Extended Data Fig. 5n, the peak $\Delta F/F_0$ of a single spine Ca^{2+} transient was compared immediately before and after the spike to measure Ca^{2+} spike-induced changes.

Spine diameter analyses was performed according to previous studies⁴⁷. To correct for varying imaging conditions, the ratio of spine head diameter to adjacent dendritic shaft diameter was used to measure spine head diameter in tuft dendrites expressing both GCaMP6s and tdTomato. After background subtraction, the fluorescence intensity of the spine (the intensity of all pixels covering the spine in the best focal plane) was divided by the fluorescence intensity of the adjacent dendritic shaft. We measured spine head diameter before Ca^{2+} spike generation, 2 min and 40 min after spikes in active spines and non-active spines on the same dendritic segment (Fig. 2g, h). Spine size change was calculated by comparing spine size measurement 2 or 40 min after spikes to the first spine size measurement (before spikes).

Ca^{2+} activities in L5 trunk and soma were measured according to recently-published studies²⁰. Task-specific apical trunk (Fig. 1j, l) and somata (Extended Data Fig. 3b–d) were defined as ROIs that showed activity (one or more transients) in one task but not in the other. In Fig. 5 and Extended Data Fig. 9c, e, GCaMP6s fluorescence changes over 20 and 40 min from individual L5 neurons was quantified as averaged $\Delta F/F_0$ over 2.5-min period of running after each training block. **Statistical analyses.** All imaging and behavioural data were presented as mean \pm s.e.m. Student's *t*-test (two-tailed) was used to test for differences between groups whose distributions passed tests for normality (Kolmogorov–Smirnov). Wilcoxon matched-pairs signed rank test and Mann–Whitney *U* test were used to analyse those groups whose distributions did not pass tests for normality. Significant levels were set at $P \leq 0.05$. All statistical analyses were performed using the GraphPad Prism. Statistical details for the experiments described in Figs 1–5 are detailed below, including the sample size (number of dendrites, spines, neurons and number of mice). Sample sizes were chosen to ensure adequate power with the statistical tests while minimizing the number of animals used in compliance with ethical guidelines. Experiments did not involve randomization or blinding because no dendritic spikes, potentiated or depotentiated spines, or behavioural performance of animal groups were predefined.

For comparing changes in steady run gait during training in Fig. 1c, the distance between adjacent footprints was measured with ink over 5 trials before and after two 2-min training blocks from 9 mice. Normalized average stride length: 1 ($t = 0$ –5 min), 1.3 ± 0.06 ($t = 25$ –30 min, $P = 0.0003$, paired Student's *t*-test), 1.6 ± 0.07 ($t = 50$ –55 min, $P = 0.0004$, paired Student's *t*-test).

The number of apical tuft Ca^{2+} spikes during forward or backward running in Fig. 1f was compared to quiet resting state in L3 mice expressing GCaMP2.2c. Fold change was calculated from the average number of spikes over 2.5 min recording within an imaging window of $160 \mu\text{m}$ by $80 \mu\text{m}$. Forward run: 24.5 ± 2.4 versus quiet resting: 2.4 ± 0.4 , $P = 2.5 \times 10^{-7}$, paired Student's *t*-test. Backward run: 19.7 ± 1.7 versus quiet resting, $P = 2.6 \times 10^{-7}$, paired Student's *t*-test.

Distribution of Ca^{2+} spike peak amplitude in Fig. 1h was measured during forward running. GCaMP6s: $n = 141$ spikes from 9 mice; peak amplitude was $945 \pm 51\%$. GCaMP2.2c: $n = 213$ spikes from 5 mice; peak amplitude was $111.9 \pm 3.9\%$. GCaMP2.2c with local MK801 applied to layer 1: $n = 31$ spikes from 4 mice; peak amplitude was $42.7 \pm 3.4\%$. The peak amplitude of Ca^{2+} spikes detected by GCaMP2.2c is significantly reduced in the presence of MK801 ($P < 0.0001$; Mann–Whitney test).

Mean percentage change in the peak amplitude of dendritic spine Ca^{2+} transients in Fig. 2c was measured under various conditions. Forward running spike-induced potentiation: $74.7 \pm 7.3\%$ increase in peak $\Delta F/F_0$ ($n = 80$ spines from 9 mice (G6s) and 12 mice (G2.2c), $P < 0.001$, Wilcoxon matched-pairs signed rank test; also see Extended Data Fig. 5m, n). Backward running spike-induced potentiation: $52.7 \pm 10.9\%$ increase in peak $\Delta F/F_0$ ($n = 18$ spines from 4 mice, $P = 0.0002$, paired Student's *t*-test). Spines not active at the spike generation: $1.8 \pm 5.8\%$ increase in peak $\Delta F/F_0$ ($n = 22$ spines from 5 mice, $P = 0.76$, paired Student's *t*-test). Active spines with no encounter of spikes: $4.2 \pm 2.9\%$ increase in peak $\Delta F/F_0$ ($n = 35$ spines from 9 mice, $P = 0.15$, paired Student's *t*-test). Local application of MK801: $0.2 \pm 3.5\%$ increase in peak $\Delta F/F_0$ ($n = 31$ spines from 4 mice, $P = 0.95$, paired Student's *t*-test). Local KN-93: $6.2 \pm 5.3\%$ increase in peak $\Delta F/F_0$ ($n = 20$ spines from 3 mice, $P = 0.26$, paired Student's *t*-test). Local KN-62: $3.9 \pm 5.4\%$ increase in peak $\Delta F/F_0$ ($n = 18$ spines from 3 mice, $P = 0.48$, paired Student's *t*-test). ACSF control: $39.5 \pm 11.3\%$ increase in peak $\Delta F/F_0$ ($n = 17$ spines from 2 mice, $P = 0.003$, paired Student's *t*-test). The degrees of spine potentiation under various conditions were compared and shown in Fig. 2c (unpaired Student's *t*-test).

Correlation of peak amplitude of spine Ca^{2+} transients and peak amplitude of Ca^{2+} spike for dendrites expressing GCaMP6s ($n = 30$, $R = 0.61$, Pearson correlation coefficient, $P = 0.0003$) and GCaMP2.2c ($n = 51$, $R = 0.68$, Pearson correlation coefficient, $P < 0.0001$) in Fig. 2d.

Correlation of peak amplitude of spine Ca^{2+} transients and the spine head and shaft fluorescence ratio for dendrites expressing GCaMP6s ($n = 30$, $R = 0.65$, Pearson correlation coefficient, $P = 0.0001$) and GCaMP2.2c ($n = 51$, $R = 0.73$, Pearson correlation coefficient, $P < 0.0001$) in Fig. 2e.

The mean percentage change in the peak amplitude of spine Ca^{2+} transients in Fig. 2f was measured over 40-min training in spines active at the time of spike generation and in spines not active at the time of spike generation. Ca^{2+} spikes induced potentiation of spine Ca^{2+} transients: $53.1 \pm 10.3\%$ (0–2 min, $P = 2.2 \times 10^{-5}$, paired Student's *t*-test), $51.8 \pm 8.9\%$ (20 min, $P = 3.6 \times 10^{-6}$, paired Student's *t*-test), $47.6 \pm 10.5\%$ (40 min, $P = 0.0003$, paired Student's *t*-test) ($n = 28$ spines from 6 mice). Non-active spines at spike: $-2.0 \pm 5.4\%$ (0–2 min, $P = 0.67$, paired Student's *t*-test), $8.6 \pm 5.3\%$ (20 min, $P = 0.08$, paired Student's *t*-test), $-2.6 \pm 4.7\%$ (40 min) ($n = 17$ spines, $P = 0.53$, paired Student's *t*-test).

In tuft dendrites co-expressing GCaMP6s and tdTomato in Fig. 2h, spines undergoing Ca^{2+} spike-induced Ca^{2+} potentiation were measured for spine size changes at 40 min: $32.3 \pm 11.1\%$ ($n = 8$ spines from 5 mice, $P = 0.02$, paired Student's *t*-test); at 2 min: $2.1 \pm 7.1\%$ ($n = 11$ spines from 11 mice, $P = 0.77$, paired Student's *t*-test). Spine size change of inactive spines was measured at 40 min: $4.0 \pm 7.6\%$ ($n = 14$ spines from 5 mice, $P = 0.61$, paired Student's *t*-test); at 2 min: $0.6 \pm 4.5\%$ ($n = 23$ spines from 11 mice, $P = 0.89$, paired Student's *t*-test). The size change between active and inactive spines was also compared (unpaired Student's *t*-test) and shown in Fig. 2h.

The mean percentage change in peak amplitude of spine Ca^{2+} transients in Fig. 3c was measured in forward running periods in this task-switching task (forward–backward–forward). Spines active < 5 s before the spike induced during backward running: $-38.6 \pm 4.1\%$ change in spine peak $\Delta F/F_0$ (ratio of the fluorescent intensity between spine heads and neighbouring shafts was 0.53 ± 0.03 during backward running-induced spike, $n = 18$ spines from 8 mice, $P = 4.1 \times 10^{-5}$, paired Student's *t*-test); Spines active > 5 s before the spike: $-4.9 \pm 3.4\%$ decrease in peak $\Delta F/F_0$ ($n = 31$ spines from 8 mice, $P = 0.16$, paired Student's *t*-test); Active spines without encountering spikes: $1.8 \pm 5.0\%$ increase in peak $\Delta F/F_0$ ($n = 31$ spines from 5 mice, $P = 0.66$, Wilcoxon matched-pairs signed rank test); Local application of MK801 in layer 1: $-3.7 \pm 3.2\%$ decrease in peak $\Delta F/F_0$ ($n = 34$ from 3 mice, $P = 0.26$, Wilcoxon matched-pairs signed rank test). The percentage change between active and inactive spines was also compared (unpaired Student's *t*-test) and shown in Fig. 3c.

No correlation between the percentage change in the peak amplitude of spine Ca^{2+} transients and dendritic Ca^{2+} spike amplitude in Fig. 3d ($n = 31$ spines, $R = -0.17$, $P = 0.35$).

In vivo two-photon imaging of the same cortical region in Fig. 4a reveal a substantial loss of layer 2/3 SST interneurons 2 days after diphtheria toxin treatment in SST-IRES-Cre/Rosa26-stop-iDTR mice infected with AAV-CAG-Flex-GFP viruses. Total cell number before deletion: 877 cells; total cell number after deletion: 222 cells ($n = 5$ mice, $P = 2 \times 10^{-5}$, paired Student's *t*-test).

In vivo analysis in Fig. 4b of DREADD-induced silencing of SST neurons 20 min after CNO treatment. To assess the change in Ca^{2+} response after CNO treatment in layer 2/3 SST interneurons, averaged calcium activity over 1 min during quiet resting state was measured before and after CNO application (before: 1 ; after: 0.8 ± 0.05 ; $n = 27$ somata from 4 mice, $P < 0.0001$, Wilcoxon matched-pairs signed rank test).

Control mice and mice with SST neuron deletion (SST/DTR) or silencing (SST/hM₄Di) were subjected to both forward and backward running and Ca^{2+} spikes were recorded in layer 1 over 5 trials in each direction in Fig. 4d. Overlap index was calculated by dividing the number of Ca^{2+} spikes on branches that activated during both forward/backward running trials by the number of Ca^{2+} spikes detected on branches that activated during forward or backward or both running trials. SST-intact overlap index: $9.8 \pm 1.2\%$ ($n = 12$ mice, 107 overlapping spikes out of 987 spikes); SST-intact + diphtheria toxin overlap index: $7.1 \pm 2.3\%$ ($n = 3$ mice, 13 overlapping spikes out of 197 spikes); SST/DTR + diphtheria toxin overlap index: $42.3 \pm 4.0\%$ ($n = 8$ mice, 642 overlapping spikes out of 1,470 spikes), significantly higher than SST-intact + diphtheria toxin overlap index ($P = 0.0055$, Mann–Whitney *U* test); SST/hM₄Di + saline overlap index: 4.5 ± 2.4 ($n = 6$ mice, 14 overlapping spikes out of 215 spikes) SST/hM₄Di + CNO overlap index: 39.5 ± 6.3 ($n = 6$ mice, 331 overlapping spikes out of 757 spikes, $P = 0.002$, paired Student's *t*-test).

In Fig. 4i, the mean percentage change of Ca^{2+} transient peak amplitude in previously forward-running potentiated spines after either forward or backward running in control and SST-deleted mice. Percentage change in spine $\Delta F/F_0$ in SST-intact control mice, after forward running: $4.2 \pm 2.9\%$ ($n = 35$ spines, $P = 0.15$, paired Student's *t*-test), and after backward running: $5.7 \pm 5.6\%$ ($n = 18$ spines, $P = 0.32$, paired Student's *t*-test). Percentage change in spine $\Delta F/F_0$ in SST-deleted mice, after forward running (potentiated): $14.9 \pm 6.1\%$ ($n = 24$ spines, $P = 0.02$, paired Student's *t*-test), and after backward running (depotentiated): $-20.5 \pm 10.0\%$ ($n = 34$ spines, $P = 0.016$, Wilcoxon matched-pairs signed rank test).

Mean number of tuft Ca^{2+} transients over a 30-s running trial was measured in transgenic mice expressing GCaMP2.2c in Fig. 5b. ACSF to L1: 11.6 ± 0.8 ($n = 46$ trials from 3 mice); TTX to L1: 0.38 ± 0.1 ($n = 40$ trials from 3 mice, $P < 0.0001$, Mann–Whitney *U* test); TTX to L5: 20.4 ± 0.8 ($n = 61$ trials from 3 mice, $P < 0.0001$, Mann–Whitney *U* test); mean number of trunk Ca^{2+} transients over a 30-s running trial was measured in mice expressing GCaMP2.2c. ACSF to L1: 16.8 ± 1.8 ($n = 28$ trials from 5 mice); TTX to L1: 1.8 ± 0.2 ($n = 32$ trials from 3 mice, $P < 0.0001$, Mann–Whitney *U* test); TTX to L5: 13.4 ± 1.1 ($n = 36$ trials from 5 mice), comparable to ACSF to L1: 16.8 ± 1.8 ($P = 0.2771$, Mann–Whitney *U* test).

Normalized peak $\Delta F/F_0$ of L5 somata over a 30-s running trial in Fig. 5c. ACSF applied to L1: $124.5 \pm 6.1\%$ $\Delta F/F_0$ ($n = 123$ somata from 5 mice); TTX to L1: $52.1 \pm 2.5\%$ $\Delta F/F_0$ ($n = 133$ from 3 mice, $P < 0.0001$, Mann–Whitney *U* test); TTX to L5: $14.6 \pm 4.8\%$ $\Delta F/F_0$ ($n = 60$ from 2 mice), significantly lower than ACSF to L1: $124.5 \pm 6.1\%$ ($P < 0.0001$, Mann–Whitney *U* test).

In Fig. 5e, the mean percentage change in peak amplitude of the apical trunk nexus in control and SST-deleted mice after the initial forward running (SST-intact: $63.9 \pm 8.4\%$, $n = 64$ trunk from 5 mice, $P = 3.1 \times 10^{-11}$, paired Student's *t*-test; SST-deleted: $82.3 \pm 15.8\%$, $n = 64$ from 3 mice, $P < 0.0001$, Wilcoxon matched-pairs signed rank test) and the second forward running session (SST-intact: $21.9 \pm 10.6\%$, $P = 0.26$, Wilcoxon matched-pairs signed rank test; SST-deleted: $23.7 \pm 8.6\%$, $P = 0.009$, paired Student's *t*-test). Backward running after the initial forward

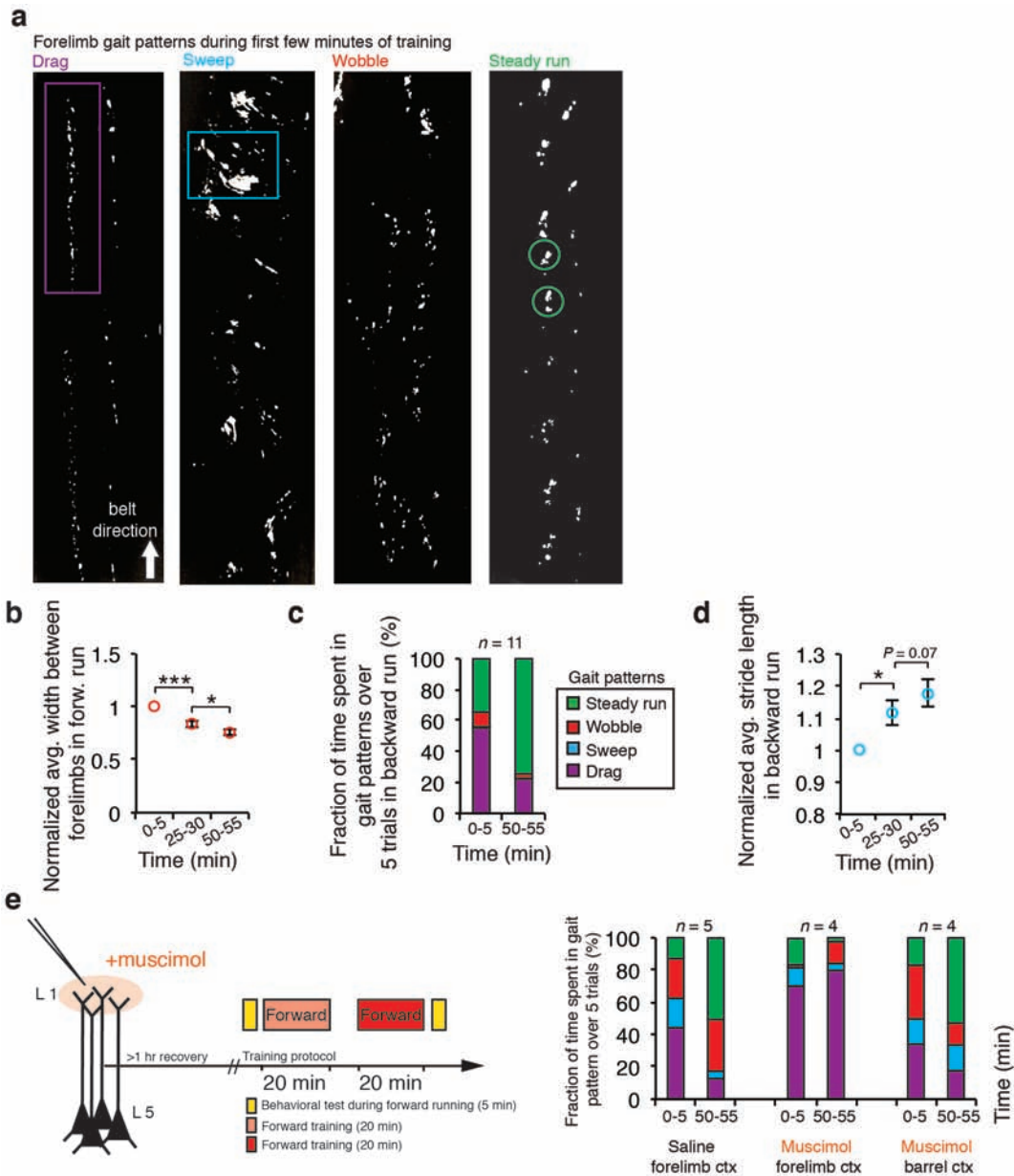
running session reduced Ca^{2+} activity at the nexus in SST-deleted mice (SST-intact: $1.0 \pm 9.2\%$, $n = 107$ from 3 mice, $P = 0.1181$, Wilcoxon matched-pairs signed rank test; SST-deleted: $-24.2 \pm 7.1\%$, $n = 77$ from 4 mice, $P = 0.001$, paired Student's *t*-test). There is a significant reduction in the trunk Ca^{2+} activity after backward running in SST-deleted mice than in SST-intact mice ($P = 0.0063$, Mann–Whitney *U* test).

In Fig. 5f, the mean percentage change in the average $\Delta F/F_0$ of L5 somata after initial (SST-intact: $23.5 \pm 2.6\%$, $n = 113$ from 6 mice, $P < 0.0001$, Wilcoxon matched-pairs signed rank test; SST-deleted: $44.4 \pm 8.6\%$, $n = 74$ from 7 mice, $P = 0.0003$, Wilcoxon matched-pairs signed rank test) and second sessions (SST-intact: $15.3 \pm 3.4\%$, $P < 0.0001$, Wilcoxon matched-pairs signed rank test; SST-deleted: $17.9 \pm 3.6\%$, $P = 9.45 \times 10^{-6}$, paired Student's *t*-test) of forward running in control and SST-deleted mice. Backward running after the initial forward running session reduced Ca^{2+} activity at L5 soma in SST-deleted mice, but not in control mice (SST-intact: $-1.0 \pm 1.6\%$, $n = 63$ from 3 mice, $P = 0.1038$, Wilcoxon matched-pairs signed rank test; SST-deleted: $-19.8 \pm 3.3\%$, $n = 67$ from 3 mice, $P = 0.0007$, paired Student's *t*-test). There is a significant reduction in L5 soma activity after backward running in SST-deleted mice than in SST-intact mice ($P < 0.0001$, Mann–Whitney *U* test).

In Fig. 5g, the mean percentage change in stride length after initial (SST-intact: $35.7 \pm 4.0\%$, $P = 1.9 \times 10^{-7}$, paired Student's *t*-test; SST-deleted: $34.4 \pm 4.9\%$, $P = 3.6 \times 10^{-6}$, paired Student's *t*-test) and second sessions (SST-intact: $22.8 \pm 3.9\%$, $P = 0.0003$, paired Student's *t*-test; SST-deleted: $17.9 \pm 3.8\%$, $P = 0.005$, paired Student's *t*-test) of forward running in control and SST-deleted mice. Backward running after the initial forward running session reduced stride length in SST-deleted mice, not in SST-intact controls (SST-intact: $14.5 \pm 5.8\%$, $P = 0.14$, paired Student's *t*-test; SST-deleted: $-25.9 \pm 6.03\%$, $P = 0.0004$, paired Student's *t*-test). There is a significant reduction in stride length after backward running in SST-deleted mice than in SST-intact mice ($P = 0.0001$, unpaired Student's *t*-test). The number of animals used under various conditions is shown in Fig. 5g.

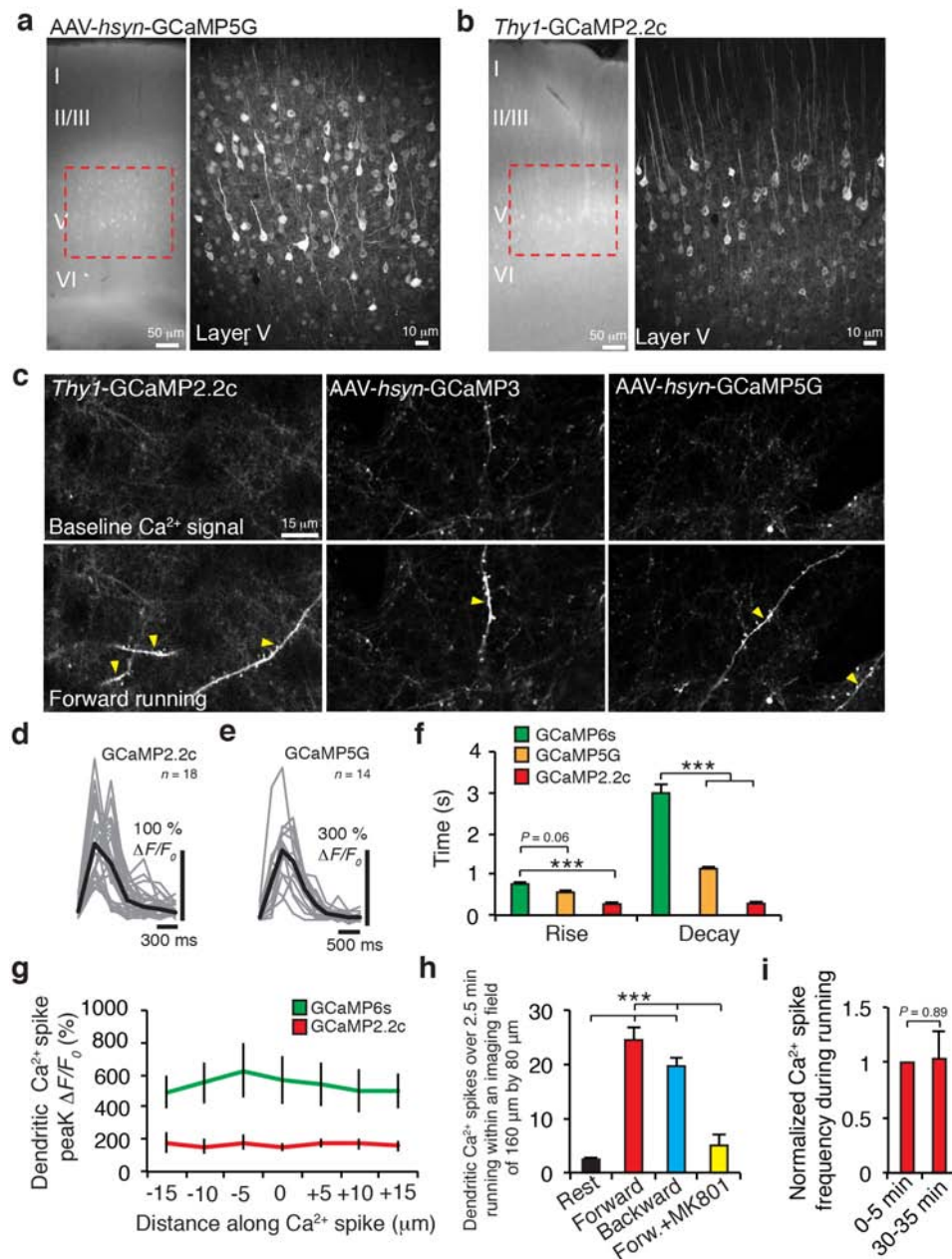
In Fig. 5h, the mean percentage change in the width between forelimbs after initial (SST-intact: $-11.2 \pm 1.9\%$, $P = 1.3 \times 10^{-5}$, paired Student's *t*-test; SST-deleted: $-17.6 \pm 2.1\%$, $P = 1.5 \times 10^{-6}$, paired Student's *t*-test) and second (SST-intact: $-4.6 \pm 1.8\%$, $P = 0.038$, paired Student's *t*-test; SST-deleted: $-4.2 \pm 3.3\%$, $P = 0.4375$, Wilcoxon matched-pairs signed rank test) sessions of forward running in control and SST-deleted mice. Backward running after the initial forward running session increased width distance in SST-deleted mice, not in SST-intact controls (SST-intact: $-4.7 \pm 1.9\%$, $P = 0.05$, paired Student's *t*-test; SST-deleted: $7.5 \pm 3.5\%$, $P = 0.04$, paired Student's *t*-test). There is a significant increase in width distance after backward running in SST-deleted mice when compared to that in SST-intact mice ($P = 0.004$, paired Student's *t*-test).

44. Chen, Q. *et al.* Imaging neural activity using Thy1-GCaMP transgenic mice. *Neuron* **76**, 297–308 (2012).
45. Yang, G., Pan, F., Chang, P. C., Gooden, F. & Gan, W. B. Transcranial two-photon imaging of synaptic structures in the cortex of awake head-restrained mice. *Methods Mol. Biol.* **1010**, 35–43 (2013).
46. Tennant, K. A. *et al.* The organization of the forelimb representation of the C57BL/6 mouse motor cortex as defined by intracortical microstimulation and cytoarchitecture. *Cereb. Cortex* **21**, 865–876 (2011).
47. Grutzendler, J., Kasthuri, N. & Gan, W. B. Long-term dendritic spine stability in the adult cortex. *Nature* **420**, 812–816 (2002).



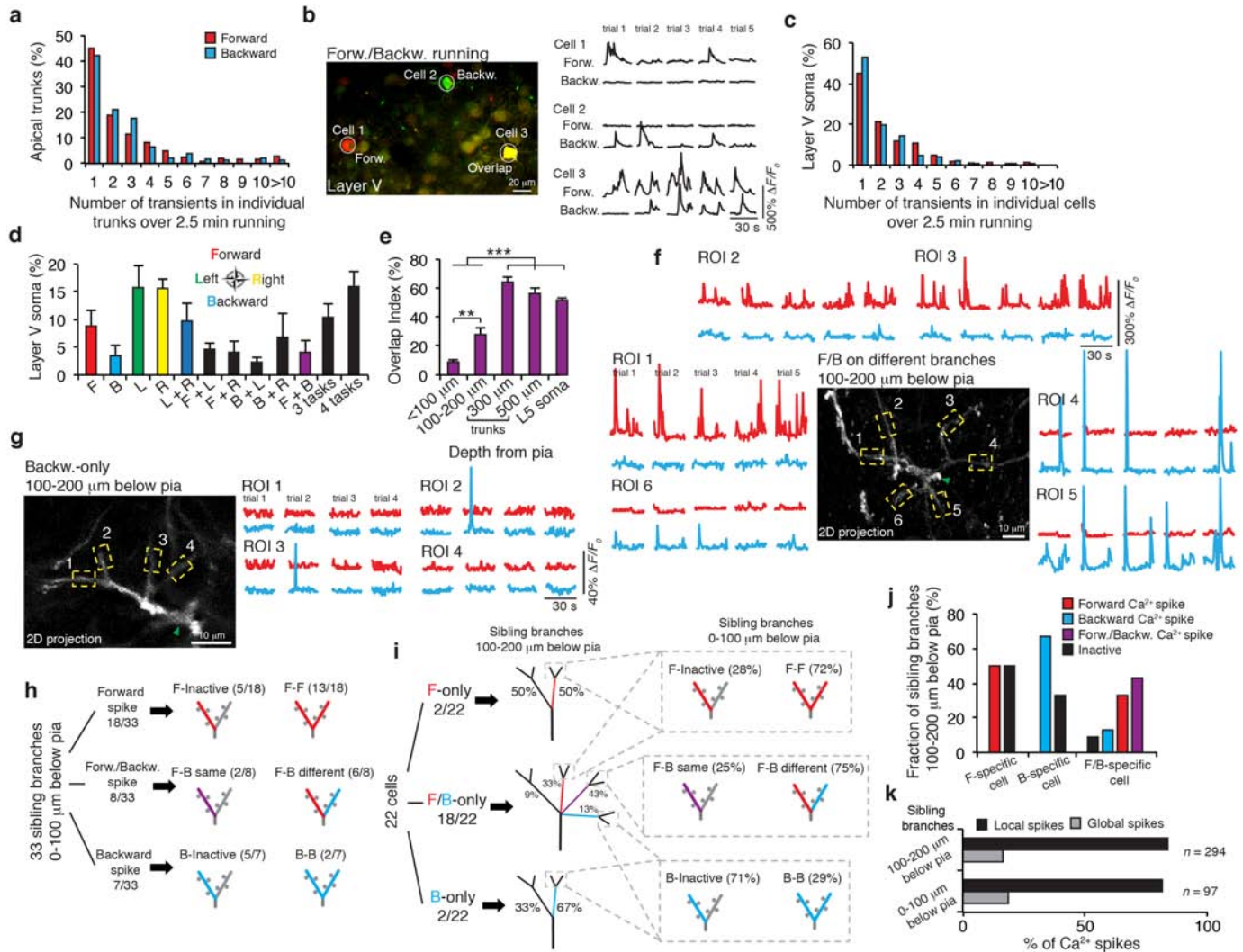
Extended Data Figure 1 | The forelimb motor cortex is important for treadmill running and performance improvement. **a**, Representative forelimb gait traces from wild-type mice running forward on the treadmill during the first few minutes of training. Several gait patterns (drag, sweep, wobble and steady run) were observed. **b**, Average width between forelimbs in steady run decreased during forward treadmill running. **c**, Backward running elicited changes in gait patterning over two 20-min training sessions. Initially, the mice exhibited mostly steady run (34%) and drag (55%) gait patterns without sweep. With continued training, mice refined their gait from drag to steady run (75%) over 40 min. **d**, Average stride length in steady run increased

during backward treadmill training. **e**, Bilateral injections of muscimol, a GABA receptor agonist, into the forelimb motor cortex acutely impaired treadmill running performance ($n = 4$). Muscimol injected mice displayed high percentages of untrained gait features (drag: 70% (0–5 min) and 80% (50–55 min)), whereas mice injected with saline to forelimb motor cortex did not (drag: 44% (0–5 min) and 13% (50–55 min)) ($n = 5$). Muscimol injections into barrel cortex did not impair treadmill running performance (drag: 34% (0–5 min) and 18% (50–55 min)) ($n = 4$). Data are presented as mean \pm s.e.m. * $P < 0.05$, *** $P < 0.001$, paired t -test.



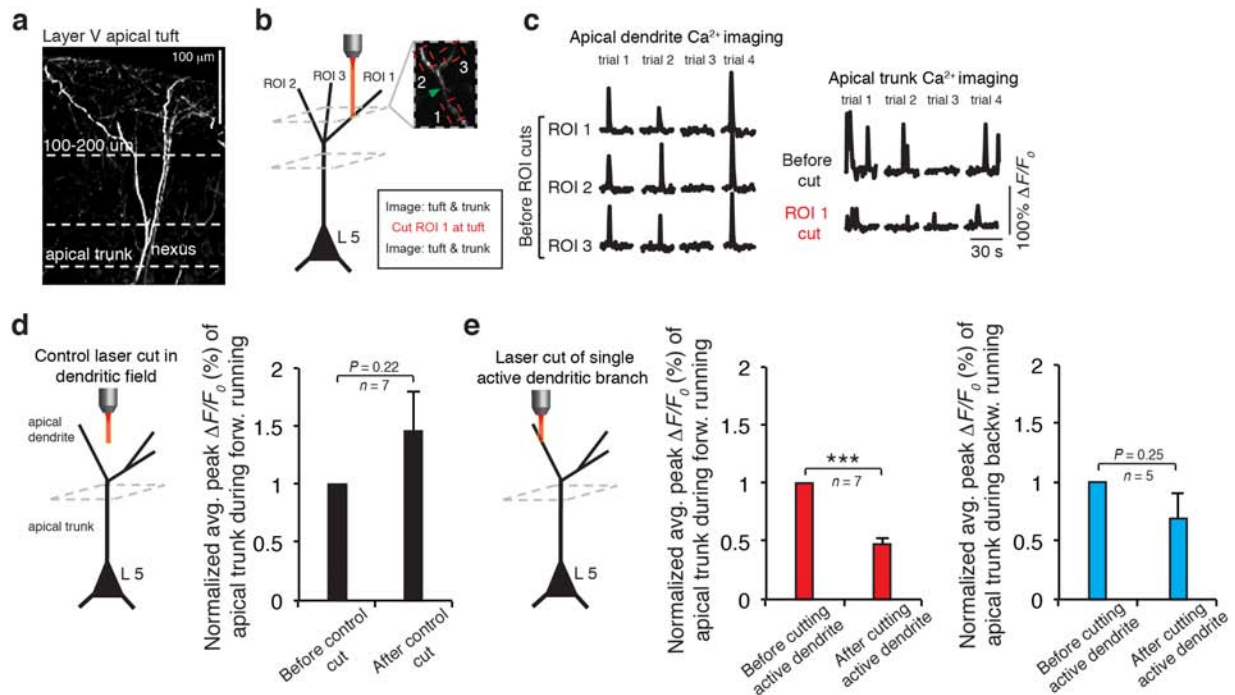
Extended Data Figure 2 | Detection of motor learning-induced Ca^{2+} spikes by various GCaMPs in apical tuft dendrites of layer 5 neurons in the motor cortex. **a, b**, Coronal sections of forelimb motor cortex from mice expressing AAV-GCaMP5G (**a**) or GCaMP2.2c (**b**). Boxed regions show the expression of GCaMPs in L5. **c**, Two-photon images of GCaMP2.2c-, 3- and 5G-expressing dendrites during quiet resting state and forward running. Images of baseline Ca^{2+} signals under quiet resting state (top) and running-induced Ca^{2+} spikes (bottom; yellow arrowheads) are shown. **d, e**, Fast-scanning of apical tuft dendrites during forward running in mice expressing GCaMP2.2c ($n = 18$) and GCaMP5G ($n = 14$). Grey traces are individual Ca^{2+} transients and black trace represents the average. **f**, Average

rise and decay times of apical tuft Ca^{2+} spikes during running for different GCaMPs (unpaired t -test). **g**, Measurements of Ca^{2+} fluorescence along long dendritic segments in the plane of imaging. Both GCaMP6s ($n = 10$) and GCaMP2.2c ($n = 7$) detected comparable fluorescent signals across entire dendritic segments. **h**, Number of Ca^{2+} spikes during quiet resting, running forward, running backward, and with local application of MK801 (paired t -test). Ca^{2+} spikes were detected on L5 tuft branches in an image field (160 \times 80 μ m) over 2.5 min in *Thy1*-GCaMP2.2c transgenic mice. **i**, The number of dendritic Ca^{2+} spikes generated in early running trials was not significantly different from that in later (30 min) running trials ($P = 0.89$, paired t -test). Scale bar, 50 μ m (**a, b**) and 15 μ m (**c**). * $P < 0.05$, *** $P < 0.001$.



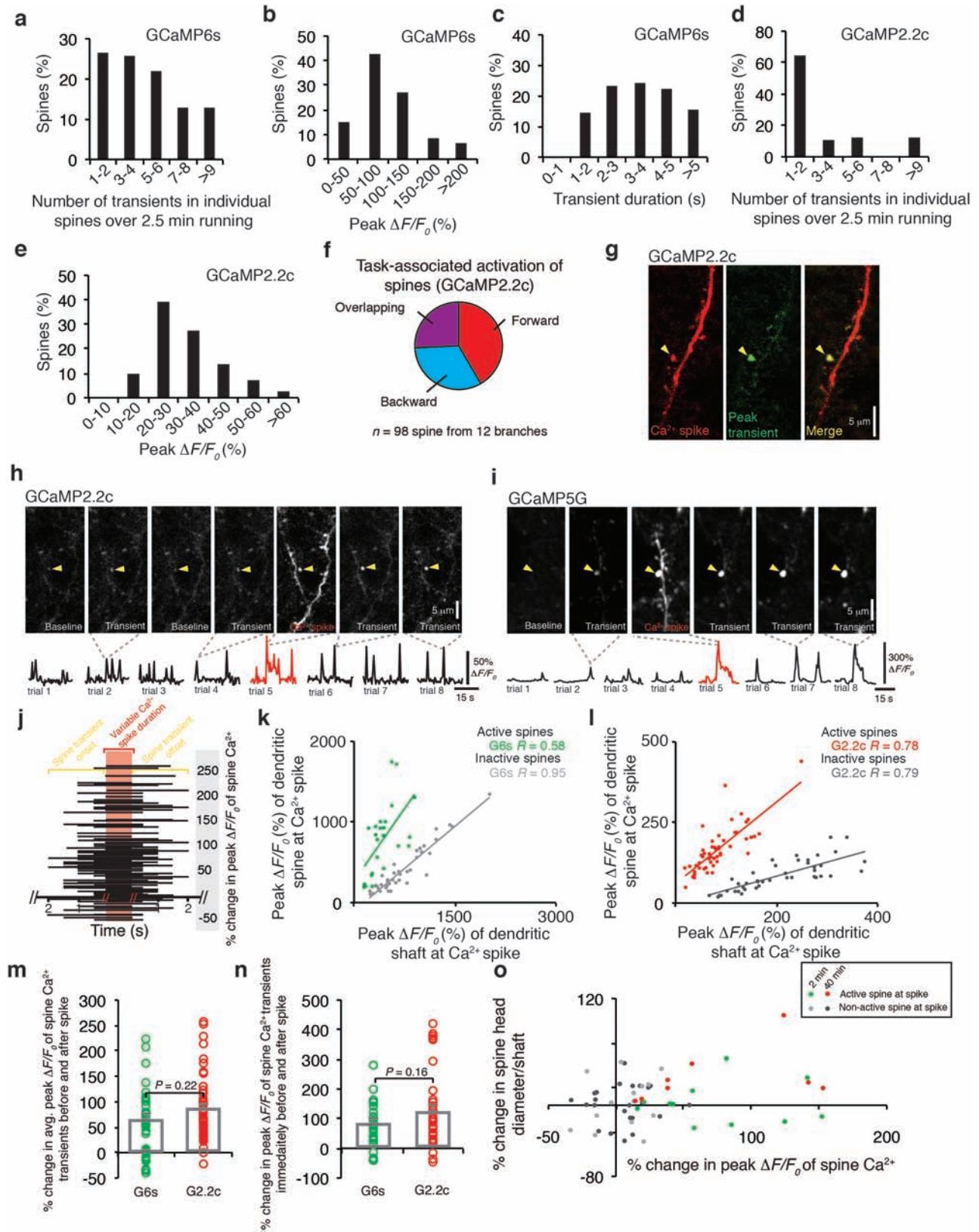
Extended Data Figure 3 | The overlap of Ca^{2+} activity in apical dendritic trunk, somata, and apical tuft branches of L5 pyramidal neurons in the motor cortex in response to treadmill running. **a**, Frequency distribution of the number of Ca^{2+} transients detected over 2.5 min in individual apical trunks in mice running forward and backward. **b**, Ca^{2+} imaging of layer 5 somata during forward and backward running. **c**, Frequency distribution of the number of Ca^{2+} transients in individual L5 somata detected over 2.5 min in mice running forward and backward ($n = 504$ cells from 10 mice). **d**, Layer 5 somata responded to multiple tasks when running in four directions ($n = 242$ cells from 4 mice). **e**, Summary of the overlap of Ca^{2+} activity in response to forward and backward running across different cortical layers in the motor cortex. **f**, Two-dimensional projection of six apical tuft branches from the same L5 neuron expressing GCaMP6s. Six ROIs corresponding to different branches were analysed over 2.5 min forward or backward running. Green arrowhead marks the location of the trunk ($\sim 200 \mu\text{m}$ below the pia). Note that there is little or no overlap between forward spikes and backward spikes in these

branches. **g**, Two-dimensional two-photon image of four apical tuft branches expressing GCaMP2.2c from an individual L5 neuron. Green arrowhead marks the trunk. Four ROIs corresponding to different branches were analysed over four trials of forward and backward running. ROI 2 and 3 generated Ca^{2+} transients in response to backward running. **h**, Distribution of forward and backward running-induced Ca^{2+} spikes on 33 sibling branches located 0–100 μm below the pia. Data were analysed over five 30-s trials of forward and backward running. **i, j**, Distribution of forward and backward running-induced Ca^{2+} spikes on 80 sibling branches located 100–200 μm below the pia (22 cells). Approximately 43% branches at this cortical depth exhibited spikes in response to both forward and backward running. Each of these branches was connected to higher order branches that were either inactive or exhibited spikes in response to forward, backward or both running modes (dotted boxes in **i**). **k**, Percentage of local or global Ca^{2+} spikes observed on sibling branches located at two different depths below the pia. $**P < 0.01$, $***P < 0.001$, unpaired t -test.



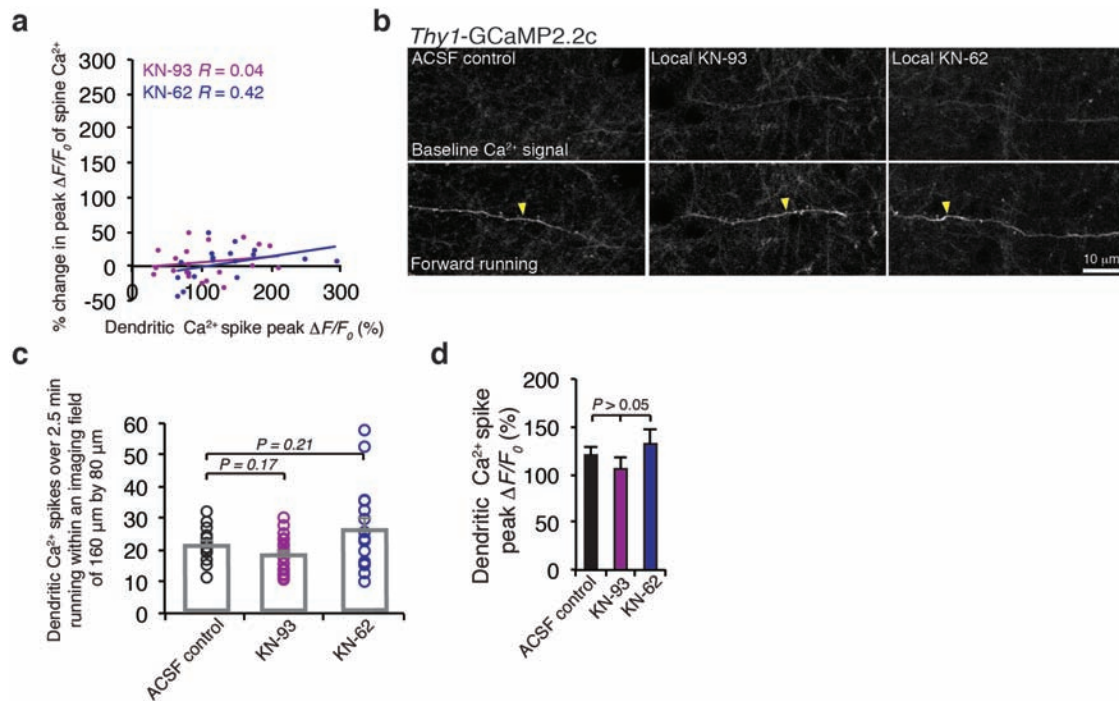
Extended Data Figure 4 | In vivo two-photon laser cutting of one apical tuft branch reduces calcium activity at the apical trunk. **a–c**, Example of an individual neuron with three apical tuft branches (at 150 μm) and the apical trunk (at 300 μm ; **a**) showed Ca^{2+} spikes during forward running. Laser cutting one tuft branch (**b**) induced a significant reduction in average peak $\Delta F/F_0$ of the trunk during forward running (**c**). **d**, Summary of average peak $\Delta F/F_0$ of the trunk before and after parking the laser beam in a region 30 μm away from the active dendrite (control cut; $n = 7$, $P = 0.22$, paired t -test). There was no significant change in the activity of the trunk in this control experiment. **e**, Summary of average peak $\Delta F/F_0$ of the trunk before and after cutting an active dendrite during forward ($n = 7$, $P < 0.001$, paired t -test) and backward

running ($P = 0.25$; $n = 5$). $***P < 0.001$. As expected, cutting a dendritic branch exhibiting forward running-induced Ca^{2+} spikes reduced the activity of the trunk when animals ran in the forward direction (left). When the branch with forward Ca^{2+} spikes was cut, the average activity of the trunk was also reduced for the backward direction (right), even though the uncut branch still exhibited Ca^{2+} spikes in response to backward running. This is probably related to the fact that apical tufted branches possess spines that are active during both forward and backward running (data not shown). Cutting a branch eliminated the contribution of not only dendritic Ca^{2+} spikes but also synaptic inputs to the depolarization at the trunk.



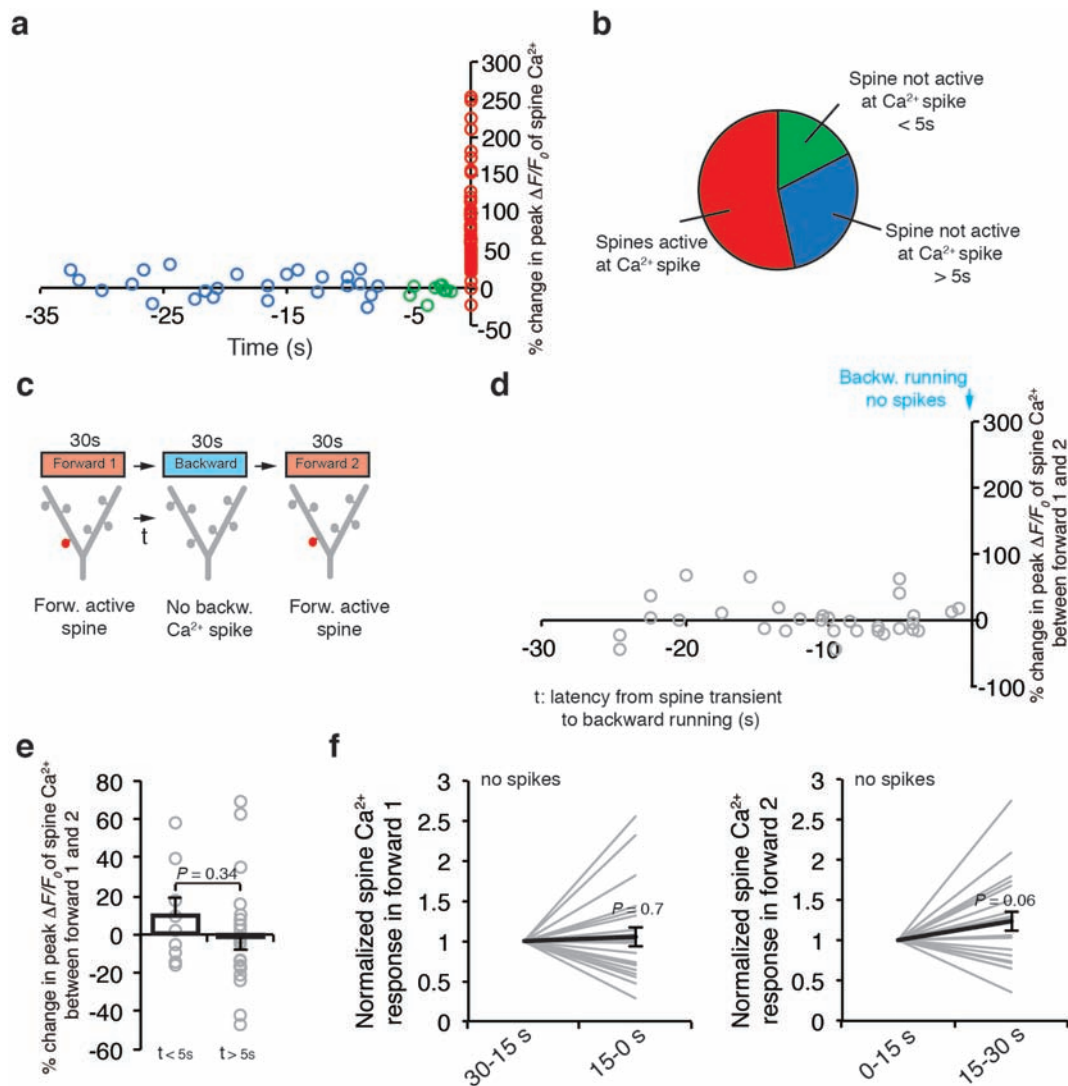
Extended Data Figure 5 | Ca^{2+} spikes cause long-lasting potentiation of task-related dendritic spines. **a**, Frequency distribution of the number of Ca^{2+} transients in individual spines detected by GCaMP6s over 2.5-min running ($n = 199$ spines from 14 dendritic branches). **b**, Frequency distribution of the peak amplitude ($\Delta F/F_0$) of spine Ca^{2+} transients on apical tuft branches expressing GCaMP6s during running. **c**, Frequency distribution of spine Ca^{2+} transient duration during running. **d**, Frequency distribution of the number of spine Ca^{2+} transients detected by GCaMP2.2c over 2.5-min running. **e**, Frequency distribution of the peak amplitude ($\Delta F/F_0$) of spine Ca^{2+} transients induced by forward running in tuft dendrites expressing GCaMP2.2c. As expected, spine Ca^{2+} transients detected with GCaMP6s were significantly higher than those detected by GCaMP2.2c in terms of amplitude ($>200\%$) and frequency ($>150\%$). **f**, Task-specific activation of dendritic spines detected by GCaMP2.2c during forward and backward running ($n = 98$ spines from 12 dendrites). **g**, Two-photon images of an apical tuft dendrite expressing GCaMP2.2c. An active spine (green) denoted by yellow arrowhead and a Ca^{2+} spike (red) are shown. **h**, **i**, Representative two-photon images and fluorescent traces of potentiated spines on L5 apical tuft dendritic segments expressing GCaMP2.2c and 5G. Ca^{2+} spikes occurred during trial 5 in **h** and **i**.

j, Many spines were active before, during and after the generation of Ca^{2+} spikes. Horizontal lines indicate the start and end of spine Ca^{2+} transients. Variable Ca^{2+} spike duration indicated by red shaded bar. **k**, **l**, Comparison of spine head and shaft fluorescence for spines active at the time of spike generation versus neighbouring spines that are not active at the time of spike generation. $\Delta F/F_0$ of active spine heads are significantly larger ($P < 0.001$; 236.5% (GCaMP6s); 319.2% (GCaMP2.2c)) than that of neighbouring inactive spines during Ca^{2+} spike generation. **m**, Percentage change in average peak $\Delta F/F_0$ of spine Ca^{2+} transients before and after spikes detected by GCaMP6s (green) and GCaMP2.2c (red). The peaks of 3–4 spine Ca^{2+} transients ($\Delta F/F_0$) were averaged before and after the spike. There was no significant difference in the degree of spine Ca^{2+} transient potentiation detected by GCaMP6s (green) and GCaMP2.2c (red) ($P = 0.22$, unpaired t -test). **n**, Percentage change in the peak $\Delta F/F_0$ of individual spine Ca^{2+} transients (no average) immediately before and after spikes detected by GCaMP6s (green) and GCaMP2.2c (red) ($P = 0.16$, unpaired t -test). **o**, Comparison of spine size versus the percentage change in the peak amplitude of spine Ca^{2+} transients at 2 min and 40 min post spike. Data are mean \pm s.e.m. Scale bars, 5 μm .



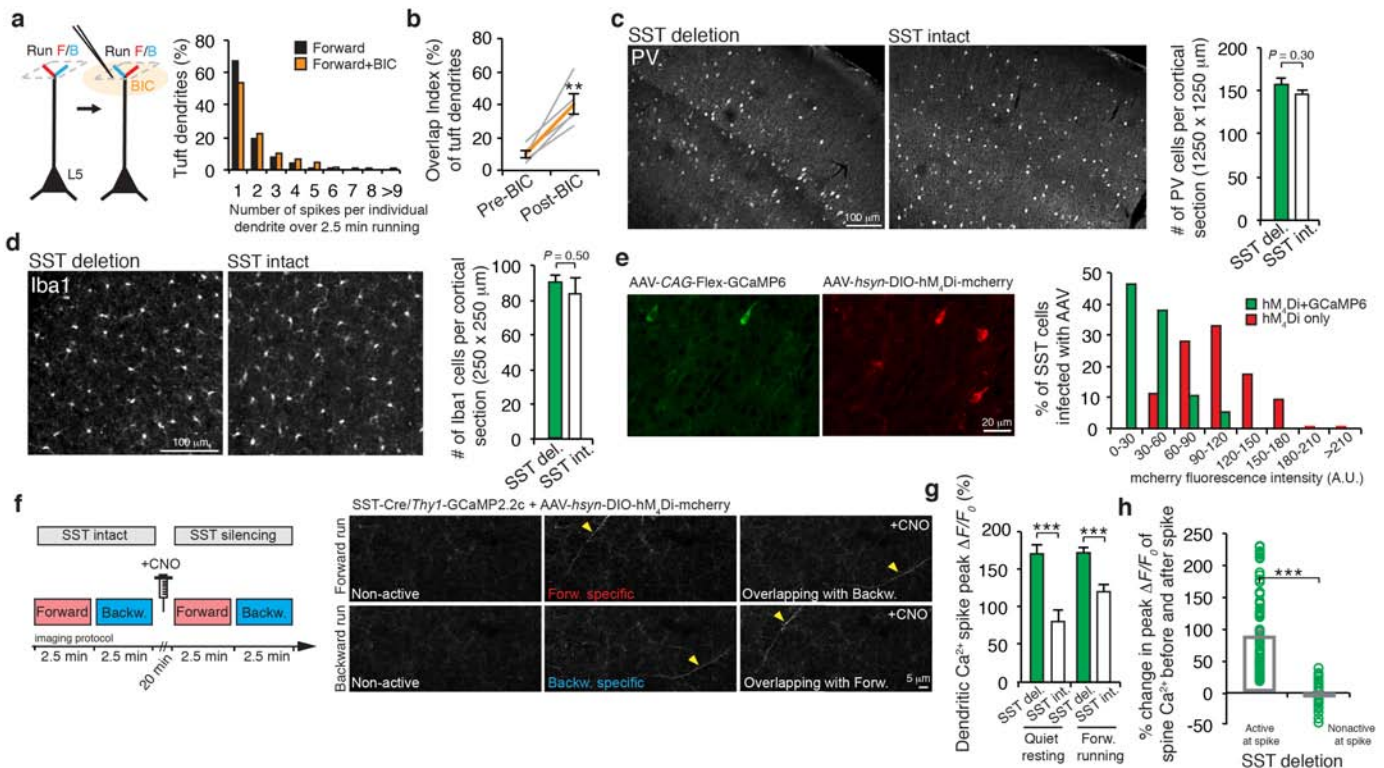
Extended Data Figure 6 | CaMKII inhibitors block potentiation of task-related dendritic spines but not Ca^{2+} spike generation. **a**, There is no correlation between the percentage change in the peak amplitude of spine Ca^{2+} transients and the peak amplitude of dendritic Ca^{2+} spike during forward running in the presence of CaMKII inhibitors (KN-62: $P = 0.08$; KN-93: $P = 0.42$, Pearson's correlation). **b**, Two-photon images of apical tuft dendrites

expressing GCaMP2.2c during quiet resting state and forward running in the presence of ACSF, KN-93 and KN-62. **c**, **d**, Local application of CaMKII inhibitors, KN-93 and KN-62, to layer 1 did not induce significant changes in Ca^{2+} spike frequency or peak amplitude as compared to ACSF controls ($P > 0.05$, unpaired t -test). Scale bar, 10 μm . Data are mean \pm s.e.m.



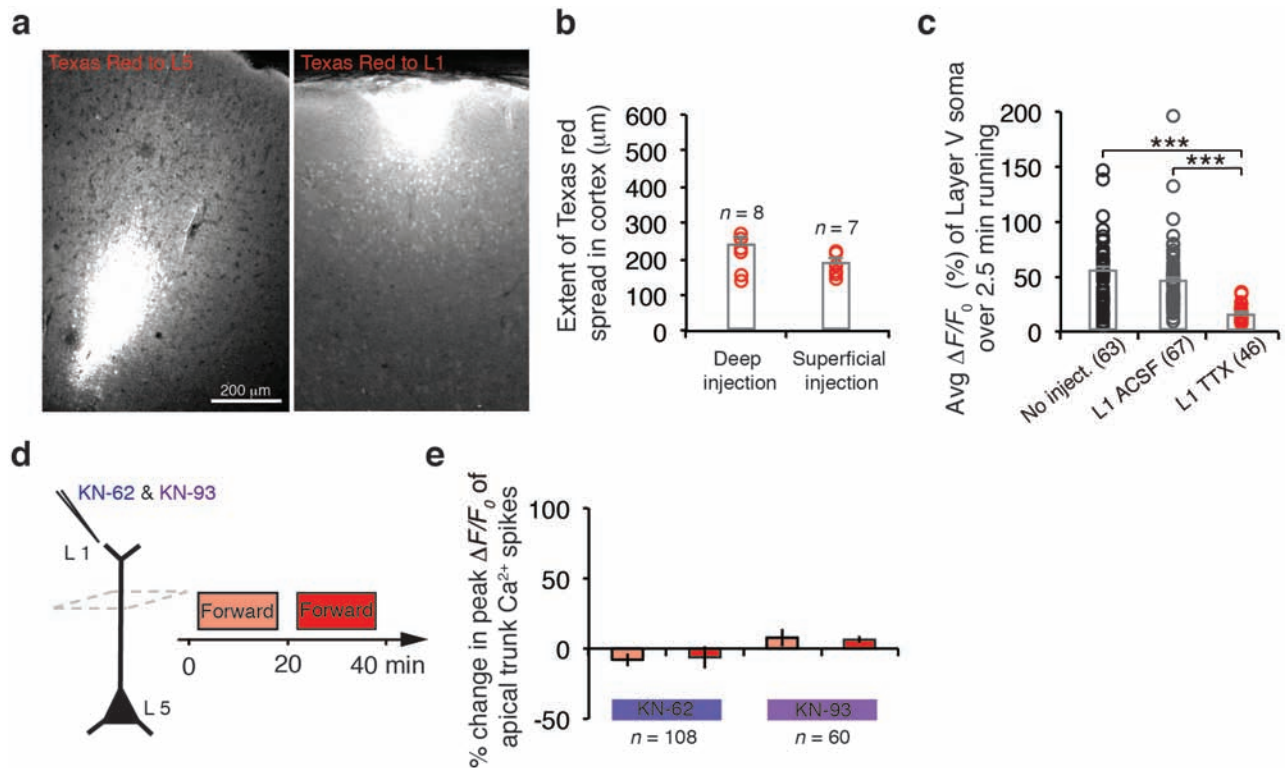
Extended Data Figure 7 | Spine activity relative to spike generation and task switching. **a, b**, In mice running forward, most spines (54%, red) exhibited activities at the time of the spike generation (near $t = 0$). Only a small fraction of spines were active < 5 s before Ca^{2+} spike generation (17%, green). Thus, most spines active during forward running coincide with the spike generation. Of the spines that were active asynchronously relative to Ca^{2+} spikes, the average time interval between the two events was 12.2 ± 1.6 s. **c, d**, Changes in the peak amplitude of Ca^{2+} transients in forward running-activated spines versus the time interval between spine activity and the onset of task switching from forward to backward running. **e**, Spines active < 5 s or > 5 s before task

switching (no backward spike) show no significant reduction in the peak amplitude of Ca^{2+} transients afterwards (< 5 s: $P = 0.31$; $n = 9$; > 5 s: $P = 0.84$; $n = 22$; unpaired t -test). **f**, There are no significant changes in the peak amplitude of spine Ca^{2+} transients (no backward spike) during the first and second half of a 30-s forward running trial, either before or after the task switching (paired t -test). Thus, spine transients do not gradually decrease during the initial forward running and recover to their highest values after the second forward running session is switched on. This suggests that the depotentiation of spines active within 5 s before spikes in Fig. 3 is related to their interactions with local Ca^{2+} spikes.



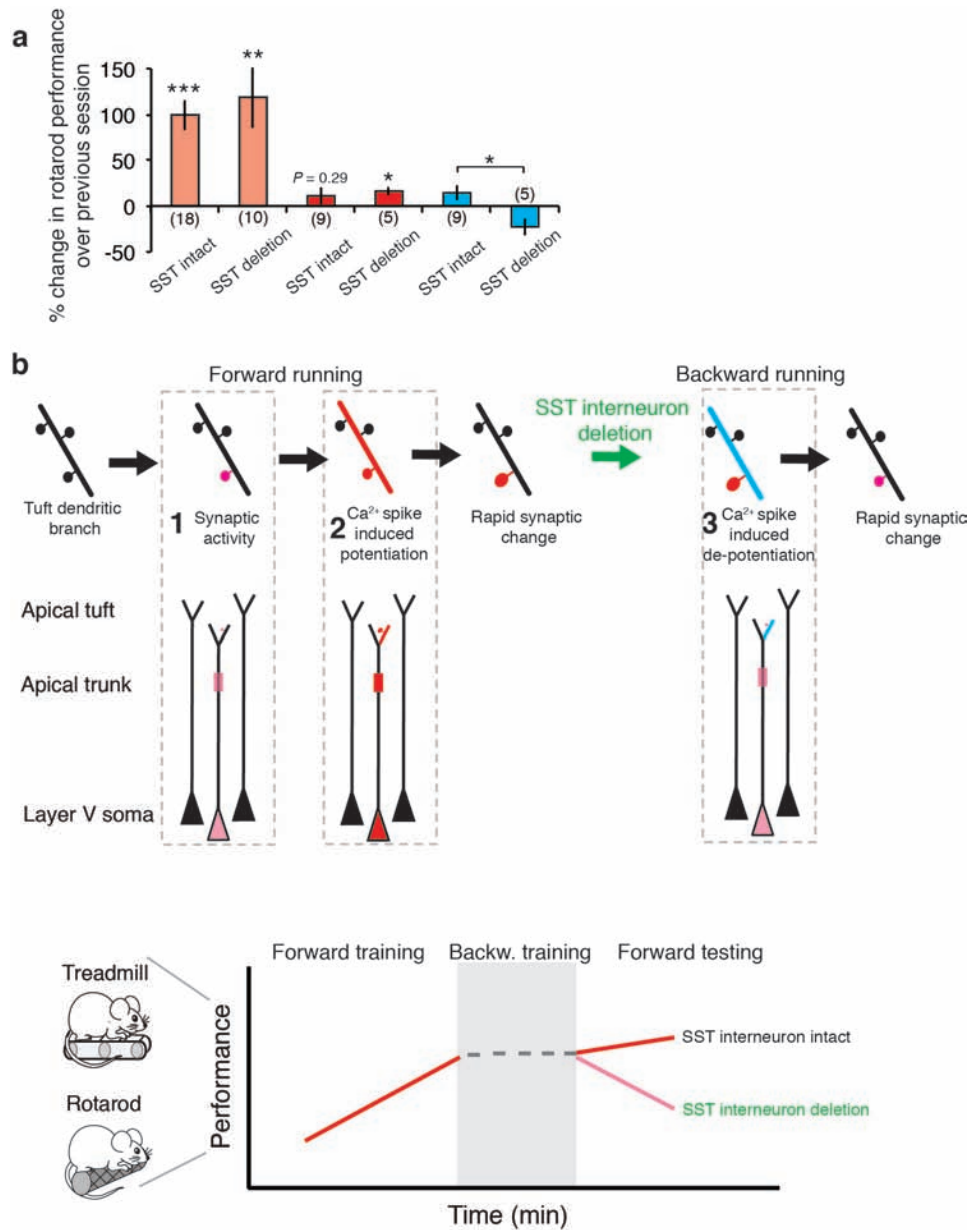
Extended Data Figure 8 | The effect of inactivating SST neurons on Ca^{2+} spikes and potentiation of task-related dendritic spines. **a**, Experimental design for perturbing branch-specific Ca^{2+} spikes by applying bicuculline (BIC) to L1. Local bicuculline administration did not have a significant effect ($P > 0.05$, paired t -test) on the number of Ca^{2+} spikes generated during forward running as compared to control mice. Before bicuculline: 60.2 ± 10.2 Ca^{2+} spikes over 2.5 min; after bicuculline application: 77.4 ± 13.7 Ca^{2+} spikes over 2.5 min. More than 200 Ca^{2+} spikes were measured under each condition from five mice. **b**, Local bicuculline administration increased the percentage of apical tuft branches exhibiting Ca^{2+} spikes during both forward and backward running ($n = 5$ mice, $P = 0.007$, paired t -test). **c**, Coronal sections of the motor cortex from control or SST-deleted mice stained for parvalbumin (PV) 2 days after diphtheria toxin administration. No significant effect on the number of parvalbumin cells was observed ($P = 0.30$, unpaired t -test). **d**, Coronal sections of motor cortex from control or SST-deleted mice stained for microglia (Iba1) 2 days after diphtheria toxin administration. No significant effect on the number of microglia was observed ($P = 0.50$, unpaired t -test). **e**, Two-photon images and quantification of SST cells expressing

GCaMP6 and hM₄Di-mCherry. **f**, Training protocol (left) to test the effect of inactivating SST cells after CNO treatment on branch-specific Ca^{2+} spike generation. Two-photon images (right) of apical tuft dendrites expressing GCaMP2.2c during forward and backward running before and after SST neuron silencing. Note that tuft dendrites after CNO exhibited Ca^{2+} spikes during both forward and backward running. **g**, The average peak amplitude of Ca^{2+} spikes during resting and running in SST-deleted and control mice expressing GCaMP2.2c. The peak $\Delta F/F_0$ of Ca^{2+} spikes during quiet resting and forward running in SST-deleted mice was significantly higher than in control mice ($P < 0.001$, unpaired t -test). **h**, In SST-deleted mice, spines active at the time of spike generation show enhanced Ca^{2+} signals after spike generation ($n = 49$, $P < 0.001$, paired t -test), whereas spines not active at the time of spike generation showed no significant increase in spine Ca^{2+} signals. In SST-deleted mice, the ratio of Ca^{2+} fluorescence intensity between spine heads and neighbouring shafts was 2.03 ± 0.23 , significantly higher than that for neighbouring inactive spines (0.61 ± 0.03). Data are mean \pm s.e.m. $**P < 0.01$, $***P < 0.001$.



Extended Data Figure 9 | CaMKII inhibitors block training-related potentiation of Ca^{2+} transients in L5 apical trunk nexus. **a**, Texas Red dye injection in L5 or L1. **b**, Fluorescence signals spread to a region with a diameter $\sim 237 \pm 19 \mu\text{m}$ in L5 and $188 \pm 10 \mu\text{m}$ in L1 respectively. There is no overlap between the sites of injection in L5 and L1. **c**, Average $\Delta F/F_0$ of L5 soma

detected by GCaMP6s over 2.5 min running under various conditions (no injection, L1 ACSF injection, L1 TTX injection) ($P < 0.001$, unpaired t -test). **d**, **e**, In control mice, local application of CaMKII inhibitors (KN-62 and KN-93) blocked the increase in Ca^{2+} transients at the apical trunk nexus after an initial and second training session of forward running.



Extended Data Figure 10 | Deletion of somatostatin-expressing interneuron impairs performance improvement after motor learning.

a, Rotarod performance in control and SST-deleted mice subjected to forward-forward running or forward-backward running. When forward running on the accelerated rotarod was followed by backward running, SST-deleted mice displayed a reduction in their performance (the average speed animals achieved) as compared to control mice when tested again in forward running ($P < 0.05$, unpaired t -test). Data are mean \pm s.e.m. **b**, A model showing the importance of BSDCS for inducing synaptic changes that affect L5 neuronal output during motor skill learning. Dendritic spines active (1, pink) at the time of spike generation (2) show enhanced Ca^{2+} activity and changes in synaptic strength (red) following the Ca^{2+} spike. Ca^{2+} spike-induced

potentiation of synapses contributes to persistent synaptic changes, potentiated Ca^{2+} activity at the apical trunk and L5 soma, as well as improvements in performance over training sessions. In control mice, different motor tasks (that is, forward, backward running) induce Ca^{2+} spikes on different tuft branches of L5 neurons (not shown). Inactivation of SST interneurons results in individual dendritic branches generating Ca^{2+} spikes in response to both tasks (3). Loss of spatial segregation of Ca^{2+} spikes results in the depotentiation of synaptic changes-induced by previous learning in tuft dendritic branches and reduced Ca^{2+} activity in the apical trunk nexus and L5 soma when a different task is learned. SST interneuron inactivation induces a state of interference that impairs motor performance when several tasks are learned.